



DIPLOMARBEIT

Proton Spectroscopy with aSPECT: Systematic Studies & Modification of the High Voltage Electrode System

Ausgeführt am
Atominstitut
der Technischen Universität Wien

unter der Anleitung von
Univ.Prof. Dipl.-Phys. Dr.rer.nat. Hartmut Abele
und
Univ.Ass. Dipl.-Math. Dr.rer.nat. Gertrud Konrad

durch

Michael David Klopf
Greiseneckergasse 11/12
1200 Wien

Wien, 17.12.2013

Ich erkläre hiermit, dass ich die eingereichte Diplomarbeit selbstständig verfasst habe und keine anderen als die angegebenen Quellen und Hilfsmittel benutzt wurden. Weiters versichere ich, dass ich diese Diplomarbeit bisher weder im In- noch im Ausland in irgendeiner Form als Prüfungsarbeit vorgelegt habe.

17.12.2013

Michael Klopf

Abstract

The decay of the free neutron offers an important possibility to test the Standard Model of particle physics with high precision measurements. Various parameters determining the decay rate of the neutron are linked over the ratio λ of the weak coupling constants. Hence, measurements of these parameters can be compared and checked for consistency.

The spectrometer *a*SPECT has been designed to determine the electron-antineutrino correlation coefficient a with a final accuracy of 0.3%. The working principle of the spectrometer is the energy selection of decay protons by a potential barrier. For the counting, the protons have to be accelerated by a system of high voltage electrodes on the detector.

So far, unexpected background problems disturbed the measurements. Therefore a new value for a could not be presented. Field emission of electrons from the electrode surfaces is most likely a reason for the background problems. In this Master thesis, the shape of the high voltage electrodes has been investigated. Based on these simulations, a new detector electrode has been built, which reduces the field at the electrode's surface by about 30% and therefore the probability for field emission.

For the evaluation of a , the magnetic field inside the spectrometer has to be known with high (10^{-4}) precision. For this reason the magnetic field is mapped before and after beam times (and in irregular intervals) with a Hall effect sensor. The measurement data of the magnetic field mapping and of the Hall probe calibration in 2011 have been analyzed and compared with former measurements. The data analysis shows that the measurement of the magnetic field with the Hall probe limits the achievable accuracy in a to 'only' 0.26%, while a lack of probe calibration (including long-term drift) presently limits the accuracy to 0.67%.

Zusammenfassung

Hochpräzisionsmessungen zum Zerfall des freien Neutrons bieten die Möglichkeit, das Standardmodell der Teilchenphysik zu überprüfen. Viele verschiedene Zerfallsparameter des Neutrons werden über das Verhältnis λ der Kopplungskonstanten der schwachen Wechselwirkung verknüpft. Dementsprechend können die Messergebnisse verglichen und auf Konsistenz überprüft werden.

Das Spektrometer *a*SPECT wurde gebaut um die Elektronen-Antineutrino-Korrelationskoeffizienten a mit einer Genauigkeit von 0.3 % zu bestimmen. Die Zerfallsprotonen werden hierfür mittels einer Potentialbarriere nach ihrer Energie selektiert. Um die Protonen, die diese Barriere überwinden, zu zählen, werden diese mittels eines Systems von Hochspannungselektroden auf detektierbare Energien beschleunigt.

Bisher konnte kein neuer Wert für a veröffentlicht werden, da unerwartete Untergrundprobleme die Messungen verfälscht haben. Wir gehen davon aus, dass hierfür unter anderem Elektronen-Feldemission von den Oberflächen der Elektroden verantwortlich ist. Im Rahmen dieser Diplomarbeit wurde die Form der Hochspannungselektrode einer genauen Untersuchung unterzogen. Basierend auf den Ergebnissen der Simulationen wurde eine neue Detektorelektrode gebaut: Die Feldstärke an deren Oberfläche konnte um 30 % gesenkt werden und dementsprechend die Wahrscheinlichkeit für Feldemission.

Zur Bestimmung von a muss das Magnetfeld innerhalb des Spektrometers mit hoher Genauigkeit (10^{-4}) bekannt sein. Daher wird das Magnetfeld mit Hilfe einer Hall-Sonde vor und nach Strahlzeiten (und in unregelmäßigen Abständen) vermessen. Die Magnetfeldmessungen und die Probenkalibrierung von 2011 wurden analysiert und mit früheren Messungen verglichen. Die Analyse hat gezeigt, dass die Messgenauigkeit der Sonde die Bestimmung von a auf 0.26 % einschränkt, während die unzureichende Probenkalibrierung (inklusive Langzeitmessungen) derzeit eine Bestimmung von a mit einer Genauigkeit von 0.67 % erlaubt.

Contents

Abstract	i
1 Introduction	3
1.1 The beta decay of the free neutron	3
1.2 The proton recoil spectrum	6
2 The retardation spectrometer <i>a</i>SPECT	11
2.1 Working principle of a MAC-E filter	11
2.2 The <i>a</i> SPECT spectrometer	13
2.3 The adiabatic transmission function	15
2.4 Evaluation of <i>a</i> from the proton recoil spectrum	16
2.5 Measuring accuracy	17
2.5.1 Dependence on the analyzing plane voltage . .	18
2.5.2 Dependence on the magnetic field	20
3 Improvement of the upper electrode system	24
3.1 Motivation for a re-design of the upper electrode system	25
3.1.1 Background problems during earlier beam times	26
3.1.2 Penning traps and Penning discharges	29
3.2 Re-design of the detector electrode	31
3.2.1 Re-design of the detector cup	32
3.2.2 Re-design of the top cover	35
3.2.3 Influence of the position on the electric field .	38
3.3 Improvement and repair of the upper $\vec{E} \times \vec{B}$ electrode	42
3.3.1 Investigation of the electric field at the edges .	42
3.3.2 Outgassing tests for STYCAST 2850 FT with catalyst 9	45
3.4 Discharge tests at worsened vacuum conditions	51
3.5 Latest status of the background measurements	54

4	Evaluation of the magnetic field measurements in 2011	56
4.1	Accuracy and stability of the MPT-141 Hall probe . .	57
4.2	Temperature effects and zero offset	61
4.3	Decrease of the magnetic field	64
4.4	Shape of the magnetic field	66
4.5	Determination of the magnetic field ratio r_B	68
4.6	Conclusion	74
5	Summary and Outlook	75
	Appendices	77
A	Detailed calculations on the measuring accuracy	78
B	Data sheets and calibrations of the Hall-effect sensors	83
	Bibliography	93

Chapter 1

Introduction

The Standard Model (SM) of particle physics is a mathematical theory that describes the weak, the electromagnetic and the strong interaction between leptons and quarks' [11]. Though the SM has been extremely successful throughout the last decades, there are some unsolved problems like for example the strong CP problem. A possible solution has been proposed in Ref. [30]. Furthermore the SM is incomplete. Hence the masses of leptons and quarks, as well as some other constants, are parameters of the theory [9] and have to be determined by experiments. Since dark matter and dark energy form more than 95 % of the universe, the SM is only valid for the remaining 4.9 % of ordinary matter [20]. For those reasons physics beyond the SM has become an important branch of research. Besides high-energy physics experiments with large accelerators, high-precision measurements provide access to subatomic physics. Current low-energy experiments dealing with the decay of the free neutron offer an approach to subatomic physics and physics beyond the SM.

1.1 The beta decay of the free neutron

A free neutron (n) decays with a mean lifetime of $(880.0 \pm 0.9)\text{s}$ [7] into a proton (p), an electron (e^-) and an electron-antineutrino ($\bar{\nu}_e$). This process of the weak interaction is known as β^- -decay:

$$n \longrightarrow p + e^- + \bar{\nu}_e + 782.3 \text{ keV} \quad (1.1)$$

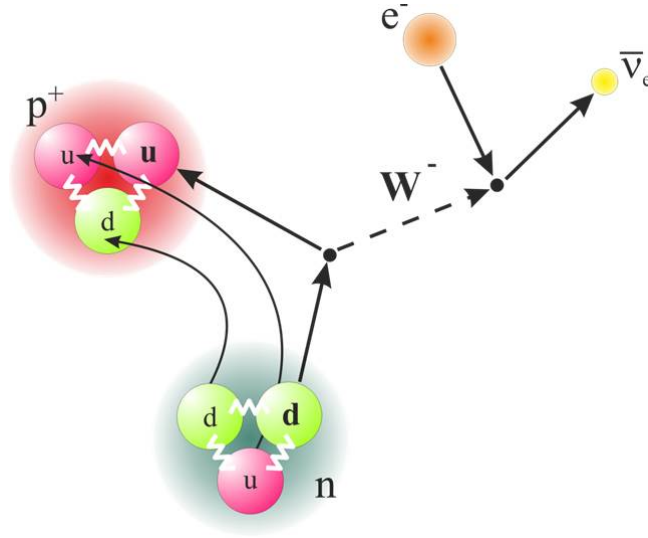


Figure 1.1: Neutron β^- -decay at the quark level: The W^- boson is the Standard Model particle that mediates the weak interaction [23].

Since the neutron and the proton are baryons, they consist of three quarks. Considering the quark flavors of the neutron (udd) and of the proton (uud), the decay reads at the quark level as

$$d \longrightarrow u + e^- + \bar{\nu}_e + 782.3 \text{ keV} \quad (1.2)$$

and is illustrated in Fig. 1.1. In the SM the differential decay rate can be written as [21]

$$\begin{aligned} \frac{d^3\Gamma}{dE_e d\Omega_e d\Omega_\nu} &= \\ &= \frac{1}{2(2\pi)^5} G_F^2 |V_{ud}|^2 (1 + 3|\lambda|^2) p_e E_e (E_0 - E_e)^2 \\ &\times \left[1 + a \frac{\vec{p}_e \cdot \vec{p}_\nu}{E_e E_\nu} + b \frac{m_e}{E_e} + \frac{\langle \vec{\sigma}_n \rangle}{\sigma_n} \cdot \left(A \frac{\vec{p}_e}{E_e} + B \frac{\vec{p}_\nu}{E_\nu} + \dots \right) \right] \end{aligned} \quad (1.3)$$

where G_F is the Fermi weak coupling constant, V_{ud} the upper left element of the Cabibbo- Kobayashi-Maskawa (CKM) quark-mixing matrix and $\lambda = g_A/g_V$ the ratio of the weak axial-vector g_A to the vector coupling constant g_V . \vec{p}_e , \vec{p}_ν , E_e and E_ν are the momenta and

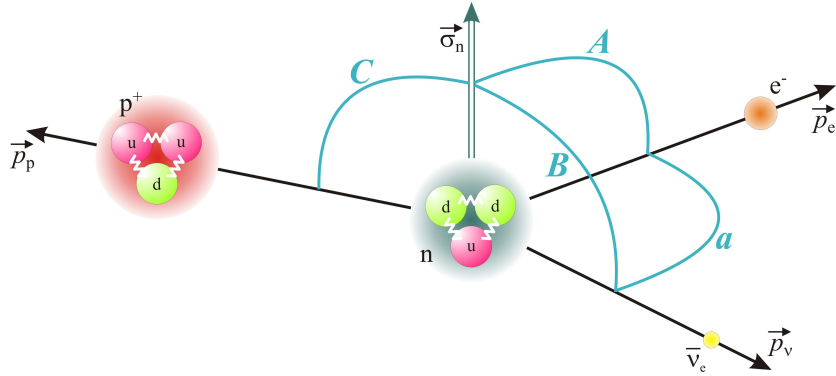


Figure 1.2: Illustration of the angular correlation coefficients a , A , B and C . $\vec{\sigma}_n$ is the neutron spin, \vec{p}_i are the momenta of the proton, electron and electron-antineutrino, respectively [23].

the total energies of the electron and of the electron-antineutrino, respectively. Furthermore, E_0 is the electron spectrum endpoint total energy, m_e the electron mass and $\vec{\sigma}_n$ the neutron spin. a , A and B are the angular correlation coefficients and are illustrated in Fig. 1.2, b is the so called Fierz interference term. In the SM, the Fierz interference term is zero. Since the terms containing A and B in Eq.(1.3) are proportional to the neutron spin $\vec{\sigma}_n$, one needs to determine these coefficients by measurements with polarized neutrons. For the determination of the electron-anti neutrino correlation coefficient a , the neutrons are not polarized. The current relative errors on a , A and B are 4 %, 0.9 % and 0.3 % [7].

The spectrometer a SPECT has been designed to measure the correlation coefficient a with high(0.3 %) accuracy [18]. The a SPECT Collaboration also plans a measurement [33]of the proton asymmetry parameter C [17]:

$$C = -x_C(A + B) , \quad (1.4)$$

where $x_C = 0.27484$ is a kinematical factor. Since the current measurements in 2013 with a SPECT aim to determine a , the focus of the following theoretical introduction is on this coefficient.

In the SM, the Fierz interference term $b=0$ and the angular correlation coefficients depend only on the ratio $\lambda = g_A/g_V$:

$$a = \frac{1 - |\lambda|^2}{1 + 3|\lambda|^2}, \quad A = -2\frac{|\lambda|^2 + |\lambda|}{1 + 3|\lambda|^2}, \quad B = 2\frac{|\lambda|^2 - |\lambda|}{1 + 3|\lambda|^2}, \quad C = x_C \frac{4\lambda}{1 + 3|\lambda|^2} \quad (1.5)$$

Since several neutron decay parameters depend only on the ratio λ , one can determine λ from different parameters and compare the derived values. This offers an important test of the validity of the SM.

Another important test of the SM is the unitarity check of the CKM quark-mixing matrix: The neutron lifetime τ_n shows the following proportionality:

$$\tau_n \propto [|V_{ud}|^2 (1 + 3|\lambda|^2)]^{-1} . \quad (1.6)$$

Hence, one can derive $|V_{ud}|$ by measuring τ_n and λ . So far, a precise determination of $|V_{ud}|$ is not possible from neutron β^- -decay as the measurements of the neutron lifetime τ_n are inconsistent [7].

1.2 The proton recoil spectrum

As mentioned in Sect. 1.1, during the last and upcoming beam times with *a*SPECT, the correlation coefficient a is to be determined with increasing precision. Considering Eq. (1.3), one sees that the term comprising a is proportional to the scalar product of the momenta of the electron and of the electron-antineutrino. Consequently, this term is proportional to the cosine of θ , the angle between the electron and the electron-antineutrino, cf. Fig. 1.3.

The electron-antineutrino interacts only weak. Hence, it is hard to detect and subsequently its momentum is difficult to determine. From a measurement of electron and proton momenta one could determine a . This, however, is not the approach of *a*SPECT: With the *a*SPECT spectrometer we measure the proton recoil spectrum. The shape of the proton recoil spectrum depends on the electron-antineutrino correlation coefficient a , as illustrated in Fig. 1.4.

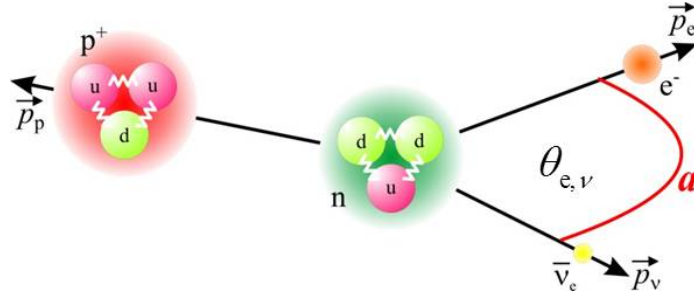


Figure 1.3: For unpolarized cold neutrons the decay rate Eq (1.7) is proportional to the cosine of the angle between the electron and the electron-antineutrino [23]

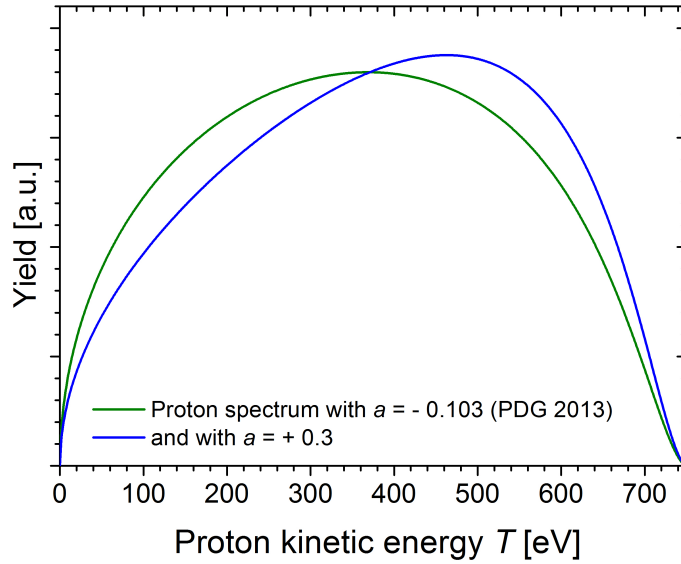


Figure 1.4: The proton recoil spectrum in neutron β^- -decay. To demonstrate the sensitivity on the electron-antineutrino correlation coefficient a , the green line shows the spectrum for the recommended value for a [7] and the blue line for a different value of a .

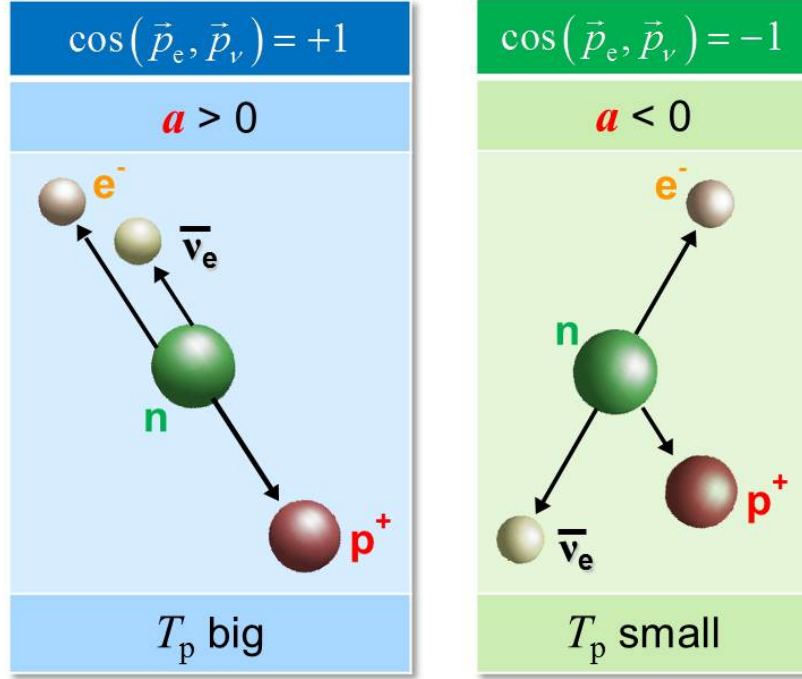


Figure 1.5: For kinematical reasons, the proton's kinetic energy depends on the angle between the electron and the electron-antineutrino.

In the SM, the Fierz interference term $b = 0$. Hence, the differential decay rate for unpolarized neutrons is given by:

$$\frac{d^2\Gamma}{dE_e d\theta_{e,\nu}} \propto \left(1 + a \frac{v_e}{c} \cos(\theta)\right) \quad (1.7)$$

If the momenta of the electron and of the electron-antineutrino point to the same direction, the proton's kinetic energy is big. Vice versa, for opposite directions, the proton's kinetic energy becomes small, as can be seen from Fig. 1.5. This is simply a consequence of energy and of momentum conservation. Hence, for a positive value of a , the first case would be preferred; and for a negative value of a , the second case would be preferred.

The theoretical proton recoil spectrum as a function of a has been calculated by Nachtmann [28]¹ and Dawber *et al.* [12]:

¹A sign error in this formula has been found by C. Habeck [19].

$$\omega_p(T) \propto g_1(T) + a \cdot g_2(T) \quad (1.8)$$

with

$$g_1(T) = \left(1 - \frac{x^2}{\sigma(T)}\right)^2 \sqrt{1 - \sigma(T)} \left[4\left(1 + \frac{x^2}{\sigma(T)}\right) - \frac{4}{3} \frac{\sigma(T) - x^2}{\sigma(T)} (1 - \sigma(T))\right] \quad (1.9)$$

$$g_2(T) = \left(1 - \frac{x^2}{\sigma(T)}\right)^2 \sqrt{1 - \sigma(T)} \left[4\left(1 + \frac{x^2}{\sigma(T)} - 2\sigma(T)\right) - \frac{4}{3} \frac{\sigma(T) - x^2}{\sigma(T)} (1 - \sigma(T))\right], \quad (1.10)$$

where T is the proton's kinetic energy and

$$\sigma(T) = 1 - \frac{2Tm_n}{\Delta^2}, \quad x = \frac{m_e}{\Delta}, \quad \Delta = m_n - m_p = 1293.333(33) \text{ keV}/c^2. \quad (1.11)$$

Here, m_n and m_p are the neutron's and the proton's mass, respectively. The functions g_1 , g_2 and $g_1 + a g_2$ are plotted in Fig. 1.6. For $a=0$ the theoretical proton recoil spectrum is only proportional to g_1 . For a non-zero value of a , the spectrum is shifted to lower or higher energies, depending on the sign of a : A positive value for a shifts the spectrum to higher energies, a negative value to lower energies.

In order to determine a , we measure the shape of the proton spectrum and extract a from a two parameter fit to the theoretical spectrum. Equation (1.8) is only an approximation for the proton recoil spectrum. For the investigation of systematic effects (cf. Chap. 2), this description of the proton recoil spectrum is sufficient. For the data analysis, additional corrections are applied. A complete list of these corrections can be found in Ref. [23], see also [15]. In the following chapter the measurement principle of a SPECT will be explained.

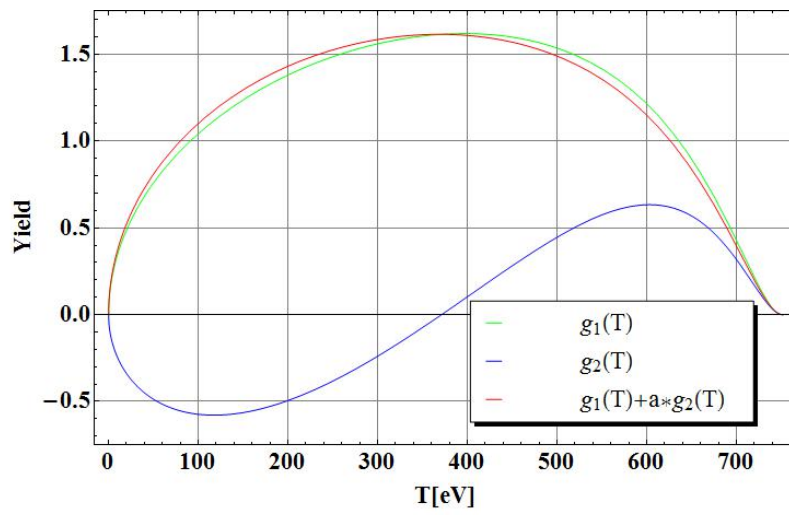


Figure 1.6: The theoretical proton spectrum for the recommended value of $a = -0.103$ [7]

Chapter 2

The retardation spectrometer *a*SPECT

The design goal of the spectrometer *a*SPECT is the measurement of the proton recoil spectrum in neutron β^- -decay, in order to determine the electron-antineutrino correlation coefficient a with a final accuracy of 0.3 %. Protons, emitted in the decay of the free neutron, gain a maximum kinetic energy of approximately 751 eV. Such energy is too low to trigger a signal at a detector. Therefore, the protons have to be accelerated to detectable energies, in the order of 10-30 kV. Necessarily, the energy determination needs to take place before the acceleration. In *a*SPECT, the energy determination is achieved through an electrostatic filter. The set-up, the working principle and the achievable measuring accuracy of *a*SPECT are presented in this chapter.

2.1 Working principle of a MAC-E filter

The measurement principle of *a*SPECT is that of a MAC-E (Magnetic Adiabatic Collimation combined with an Electrostatic Filter) filter [31]. Charged particles moving in a magnetic field \vec{B} follow the magnetic field lines. The Lorentz force \vec{F} :

$$\vec{F} = q \left[\vec{E} + (\vec{v} \times \vec{B}) \right] \quad (2.1)$$

forces them to gyrate around a magnetic field line. Here, q is the particle's charge, \vec{v} its velocity and \vec{E} an external electric field. Equat-

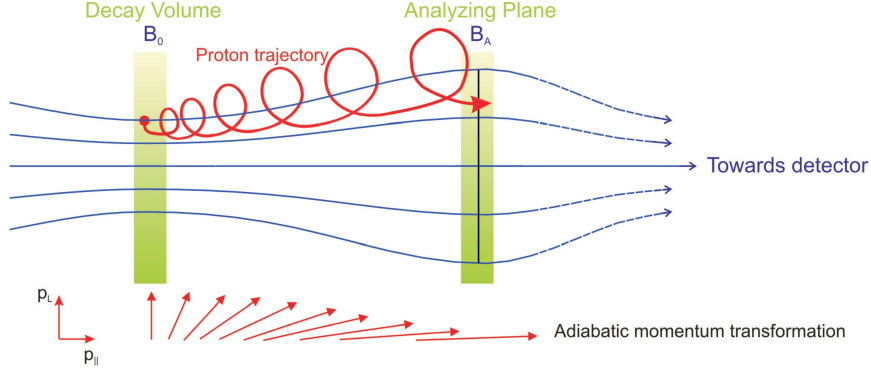


Figure 2.1: Scheme of a MAC-E filter [5]: Protons from the decay volume are guided through magnetic field lines (blue) to the analyzing plane. The analyzing plane is an imaginary plane, where both the magnetic field and the electric potential have a local maximum.

ing the Lorentz force and the centripetal force in absence of an electric field \vec{E} , one obtains for the gyration radius r :

$$r = \frac{mv_{\perp}}{qB}, \quad (2.2)$$

where m is the particle's mass and v_{\perp} the part of the particles's velocity perpendicular to the magnetic field. By reducing the magnetic field along the trajectories of the particles the transversal component of their momenta is mostly converted into the longitudinal component. This transformation needs to be adiabatic. Otherwise the mathematical description of the integral proton spectrum is impossible. The condition for adiabatic transport in a magnetic field

$$\Delta B/B \ll 1 \quad (2.3)$$

has to be fulfilled on all trajectories. Additionally to the magnetic field, an electrode system generates an electric field which serves as an electrostatic filter. Only particles with sufficient longitudinal kinetic energy can pass the electrostatic potential and will be detected afterwards. The adiabatic condition for the electric field \vec{E} is the same as for the magnetic field \vec{B} :

$$\Delta E/E \ll 1 \quad (2.4)$$

2.2 The *a*SPECT spectrometer

This description of the spectrometer *a*SPECT is based on Fig. 2.2 [23]. Unpolarized, cold neutrons (green) enter the spectrometer from the left. The neutron beam is shaped by a collimation system (for details see [8]) before it enters the decay volume (pink), where only a small fraction of the neutrons decays due to the long neutron lifetime. The decay protons (red) are guided by the strong magnetic field within the spectrometer. Protons emitted in the positive z -direction are directly guided towards the analyzing plane (brown). On the other hand, protons emitted in the negative z -direction are reflected by an electrostatic mirror (black) in order to avoid a loss of proton count rate and accomplish 100 % acceptance. The analyzing plane is an imaginary plane, where the electrostatic filter has its maximum. Only protons with sufficient longitudinal kinetic energy will overcome this electrostatic barrier and will then be accelerated onto the detector (black). To scan the shape of the proton recoil spectrum, the potential of the analyzing plane electrode, U_A , can be varied between 0 and +800 V. The maximum kinetic energy of the decay protons is approximately 751 eV. Hence, measurements at 780 V are used to characterize the background. To post-accelerate the protons to detectable energies (and to ensure that they overcome the magnetic mirror right in front of the detector) a high negative potential has to be applied to the detector. For the current setup, using a silicon drift detector (SDD), an acceleration voltage of -15 kV is sufficient [32]. By varying the analyzing plane voltage and plotting the proton count rate versus the voltage one obtains the integral proton spectrum (for details see Sect. 1.2). Actually, the electrostatic filter is not a single electrode as shown in Fig. 2.2, but a system of seven electrodes in order to accomplish adiabatic transport. The lower dipole electrode (blue) sweeps out decay protons that do not overcome the potential barrier. Otherwise they would be trapped between the analyzing plane and the decay volume. With the upper dipole electrode the neutron (proton) beam is aligned on the detector. These dipole electrodes hereafter will be referred to as $\vec{E} \times \vec{B}$ electrodes.

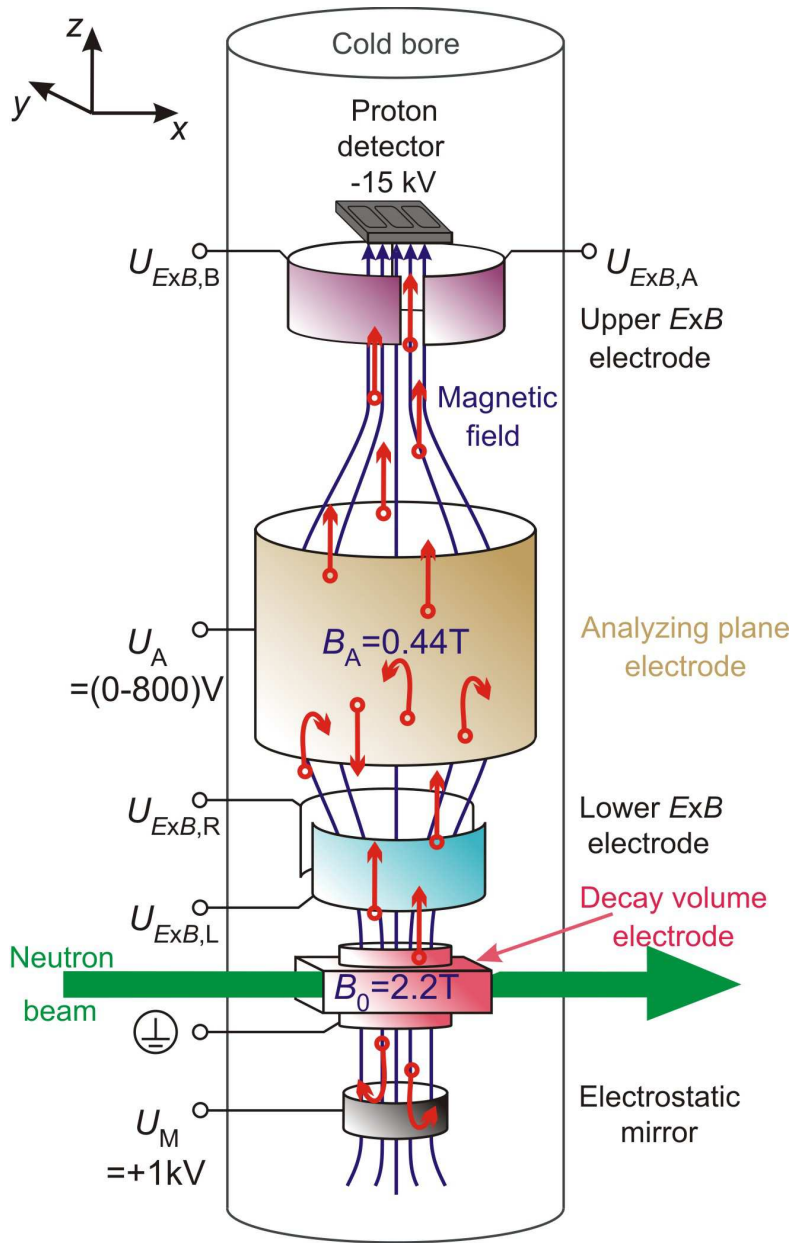


Figure 2.2: Scheme of the spectrometer *aSPECT* [23]: green: unpolarized, cold neutron beam; pink: decay volume (DV); red vectors: decay protons; gray: electrostatic mirror (for 100 % acceptance); blue: lower $\vec{E} \times \vec{B}$ electrode (sweeping out decay protons, which cannot pass the electrostatic filter); brown: electrostatic filter, referred to as analyzing plane (AP); purple: upper $\vec{E} \times \vec{B}$ electrode (aligning the neutron (proton) beam on the detector (black)).

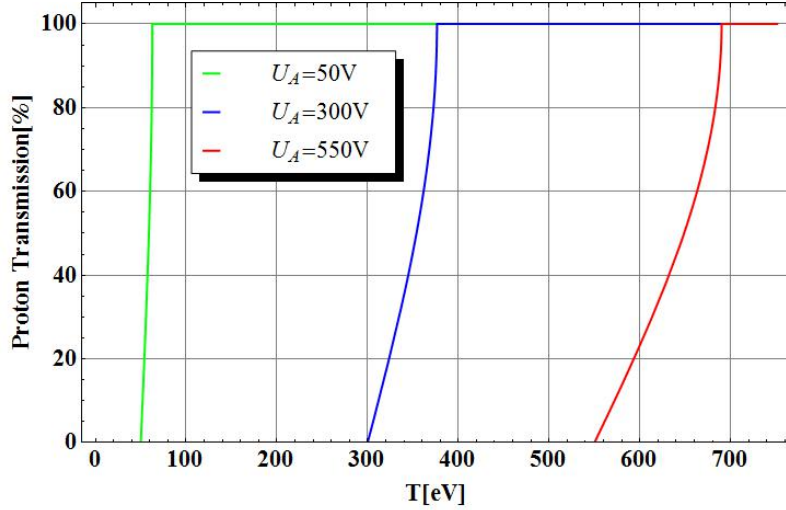


Figure 2.3: The transmission function describes the probability for a proton to overcome the electrostatic barrier, depending on its kinetic energy T . The function is plotted for three different values of the barrier voltage U_A .

2.3 The adiabatic transmission function

The transmission function describes the probability for a proton to overcome the potential barrier, depending on the proton's kinetic energy T_0 [18]¹:

$$F_{\text{tr}}(T_0; U_A) = \begin{cases} 0 & , T_0 \leq T_{\text{tr}}^{\text{min}} \\ 1 - \sqrt{1 - \frac{B_0}{B_A} \left(1 - \frac{e(U_A - U_0)}{T_0}\right)} & , T_{\text{tr}}^{\text{min}} < T_0 \leq T_{\text{tr}}^{\text{max}} \\ 1 & , T_0 > T_{\text{tr}}^{\text{max}} \end{cases} \quad (2.5)$$

with

$$T_{\text{tr}}^{\text{min}} = e(U_A - U_0) \quad \text{and} \quad T_{\text{tr}}^{\text{max}} = \frac{e(U_A - U_0)}{1 - \frac{B_A}{B_0}}. \quad (2.6)$$

Here, B_0 , B_A and U_0 , U_A are the magnetic fields respectively the electrostatic potentials in the decay volume (DV) and in the analyzing plane (AP). Since all of these parameters, except for U_A ,

¹The derivation of the transmission function has been performed in Ref. [18] and many previous theses as, e.g, Refs. [5] and [23] and is not be repeated here.

are kept constant during a measurement of the electron-antineutrino correlation coefficient a (except for systematic tests), the transmission function $F_{\text{tr}}(T_0; U_A)$ varies only with the potential applied in the AP. Figure 2.3 shows the transmission function for different analyzing plane voltages U_A .

From now on, we assume that $U_0 = 0$ in order to simplify the calculations.

2.4 Evaluation of a from the proton recoil spectrum

From the transmission function Eq. (2.5) and the theoretical proton recoil spectrum ω_p the proton count rate at the detector can be deduced. It depends only on the analyzing plane potential U_A :

$$N_p(U_A) = N_0 \int_0^{T_{p,\text{max}}} dT F_{\text{tr}}(T_0; U_A) \omega_p(T_0) . \quad (2.7)$$

Hereafter, we will use Eq. (1.8) for the theoretical proton spectrum ω_p . N_0 is the full proton count rate for 0 V in the analyzing plane. In accordance with Nachtmann (cf. Eq. 1.8), the proton recoil spectrum depends linearly on the correlation coefficient a and therefore does the proton count rate. By measuring the proton count rate for different AP potentials and subsequently applying a two parameter fit (with fit parameters N_0 and a) to the measurement data, the value of a can be determined.

Alternatively, one can determine a from the specific count rate ratio [34]:

$$r_h(U_A) = \frac{N_p(U_A)}{N_0} . \quad (2.8)$$

By substituting Eq. (2.7) and Eq. (1.8) into Eq. (2.8) we get:

$$r_h(U_A) = \frac{\int_0^{T_{p,\max}} dT F_{\text{tr}}(T; U_A) g_1(T) + a \int_0^{T_{p,\max}} dT F_{\text{tr}}(T; U_A) g_2(T)}{\int_0^{T_{p,\max}} dT g_1(T) + a \int_0^{T_{p,\max}} dT g_2(T)}. \quad (2.9)$$

Solving this equation for a yields:

$$a = \frac{\int_0^{T_{p,\max}} dT F_{\text{tr}}(T; U_A) g_1(T) - r_h(U_A) \int_0^{T_{p,\max}} dT g_1(T)}{\int_0^{T_{p,\max}} dT F_{\text{tr}}(T; U_A) g_2(T) - r_h(U_A) \int_0^{T_{p,\max}} dT g_2(T)}. \quad (2.10)$$

2.5 Measuring accuracy

As mentioned before, *a*SPECT measures the proton count rate at several barrier voltages to determine the correlation coefficient a with an accuracy of 0.3 %. a is then derived from a two parameter fit. Nevertheless we use Eq. (2.10) for an error estimation: The aim is to determine the dependency of the relative uncertainty in a on uncertainties of the potential barrier voltage U_A and of the magnetic field ratio

$$r_B = \frac{B_A}{B_0}. \quad (2.11)$$

By substituting the transmission function Eq. (2.5) into our expression for a Eq. (2.10) we obtain:

$$a = \frac{\int_{T_{\text{tr}}^{\min}}^{T_{\text{tr}}^{\max}} (1 - \sqrt{1 - \frac{B_0}{B_A} (1 - \frac{eU_A}{T})}) g_1(T) dT + \int_{T_{\text{tr}}^{\max}}^{T_{p,\max}} g_1(T) dT - r_h(U_A) \int_0^{T_{p,\max}} g_1(T) dT}{\int_{T_{\text{tr}}^{\min}}^{T_{\text{tr}}^{\max}} (1 - \sqrt{1 - \frac{B_0}{B_A} (1 - \frac{eU_A}{T})}) g_2(T) dT + \int_{T_{\text{tr}}^{\max}}^{T_{p,\max}} g_2(T) dT - r_h(U_A) \int_0^{T_{p,\max}} g_2(T) dT} \quad (2.12)$$

In order to calculate the relative uncertainties in a , we have to differentiate Eq. (2.12):

$$\frac{\Delta a}{a} = \frac{\partial a}{\partial x} \frac{\Delta x}{a} \quad (2.13)$$

where x is the potential barrier voltage U_A respectively the magnetic field ratio r_B .

We note that the integration limits in Eq. (2.12) are variable. Hence, we have to use the Leibniz integral rule for variable integration limits:

$$\frac{d}{dx} \int_{a(x)}^{b(x)} f(y, x) dy = \int_{a(x)}^{b(x)} \frac{\partial}{\partial x} f(y, x) dy + \frac{db(x)}{dx} f(b(x), x) - \frac{da(x)}{dx} f(a(x), x) \quad (2.14)$$

2.5.1 Dependence on the analyzing plane voltage

According to Eq. 2.12, we calculate a for a special value of the specific count rate ratio $r_h(U_A) = \text{const}$. Therefore the last term in the numerator of Eq. (2.12) as well as in the denominator are independent of U_A .

According to Eq. (2.14) the derivative of the first integral in the numerator of Eq. (2.12) yields

$$\frac{d(\text{Numerator})}{dU_A} = - \int_{T_{\text{tr}}^{\min}}^{T_{\text{tr}}^{\max}} \frac{e}{2r_B T \sqrt{1 - \frac{B_0}{B_A} \left(1 - \frac{eU_A}{T}\right)}} g_1(T) dT \quad (2.15)$$

Detailed calculations are in App. A.

Analogous, the derivative of the denominator yields

$$\frac{d(\text{Denominator})}{dU_A} = - \int_{T_{\text{tr}}^{\min}}^{T_{\text{tr}}^{\max}} \frac{e}{2r_B T \sqrt{1 - \frac{B_0}{B_A} \left(1 - \frac{eU_A}{T}\right)}} g_2(T) dT . \quad (2.16)$$

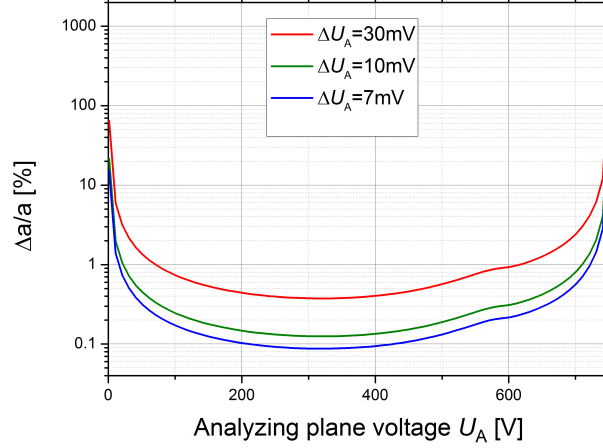


Figure 2.4: Relative uncertainty in a for an uncertainty in the analyzing plane voltage U_A of 7, 10 and 30 mV. The relative uncertainty in a strongly depends on U_A . Input data: $r_B = B_A/B_0 = 0.203$ and $a = -0.103$.

In order to differentiate Eq. (2.12), the quotient rule must be used. For the final result we obtain:

$$\begin{aligned}
\frac{da}{dU_A} = & \\
& \left\{ \left[\int_{T_{tr}^{\min}}^{T_{tr}^{\max}} \left(1 - \sqrt{1 - \frac{B_0}{B_A} \left(1 - \frac{eU_A}{T}\right)}\right) g_1(T) dT + \int_{T_{tr}^{\max}}^{T_{p,\max}} g_1(T) dT - r_h(U_A) \int_0^{T_{p,\max}} g_1(T) dT \right] \right. \\
& \times \left[\int_{T_{tr}^{\min}}^{T_{tr}^{\max}} \frac{e}{2r_B T \sqrt{1 - \frac{B_0}{B_A} \left(1 - \frac{eU_A}{T}\right)}} g_2(T) dT \right] \\
& - \left[\int_{T_{tr}^{\min}}^{T_{tr}^{\max}} \left(1 - \sqrt{1 - \frac{B_0}{B_A} \left(1 - \frac{eU_A}{T}\right)}\right) g_2(T) dT + \int_{T_{tr}^{\max}}^{T_{p,\max}} g_2(T) dT - r_h(U_A) \int_0^{T_{p,\max}} g_2(T) dT \right] \\
& \times \left. \left[\int_{T_{tr}^{\min}}^{T_{tr}^{\max}} \frac{e}{2r_B T \sqrt{1 - \frac{B_0}{B_A} \left(1 - \frac{eU_A}{T}\right)}} g_1(T) dT \right] \right\} \\
& \times \frac{1}{\left[\int_{T_{tr}^{\min}}^{T_{tr}^{\max}} \left(1 - \sqrt{1 - \frac{B_0}{B_A} \left(1 - \frac{eU_A}{T}\right)}\right) g_2(T) dT + \int_{T_{tr}^{\max}}^{T_{p,\max}} g_2(T) dT - r_h(U_A) \int_0^{T_{p,\max}} g_2(T) dT \right]^2}
\end{aligned} \tag{2.17}$$

Figure 2.4 shows the result for a deviation in U_A of 7, 10 and 30 mV². An absolute uncertainty in the AP voltage U_A of 30 mV yields a relative uncertainty in a of about 0.5 %. In order to reach the design goal of 0.3 % in a , it is necessary to keep the uncertainty in U_A below 10 mV, since there is also a dependency on the magnetic field ratio r_B , see Sect. 2.5.2.

2.5.2 Dependence on the magnetic field

The same calculations have been performed for the magnetic field ratio r_B . The derivatives of the numerator and the denominator are:

$$\frac{d(Numerator)}{dr_B} = - \int_{T_{tr}^{\min}}^{T_{tr}^{\max}} \frac{1 - \frac{eU_A}{T}}{2r_B^2 \sqrt{1 - \frac{1}{r_B} \left(1 - \frac{eU_A}{T}\right)}} g_1(T) dT \quad (2.18)$$

and

$$\frac{d(Denominator)}{dr_B} = - \int_{T_{tr}^{\min}}^{T_{tr}^{\max}} \frac{1 - \frac{eU_A}{T}}{2r_B^2 \sqrt{1 - \frac{1}{r_B} \left(1 - \frac{eU_A}{T}\right)}} g_2(T) dT . \quad (2.19)$$

For the total derivative we obtain:

²For the computation of the integrals, the numerical integration function of Mathematica 8.0 has been used, similar to Ref. [23]

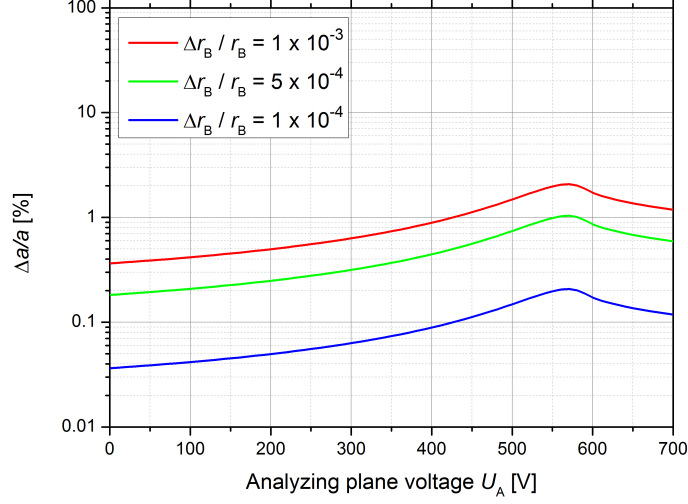


Figure 2.5: Relative uncertainty in a depending on the relative uncertainty in the magnetic field ratio $r_B = B_A/B_0$. Input data: $r_B = 0.203$ and $a = -0.103$.

$$\begin{aligned}
\frac{da}{dr_B} = & \left\{ \left[\int_{T_{tr}^{\min}}^{T_{tr}^{\max}} \left(1 - \sqrt{1 - \frac{B_0}{B_A} \left(1 - \frac{eU_A}{T}\right)}\right) g_1(T) dT + \int_{T_{tr}^{\max}}^{T_{p,\max}} g_1(T) dT - r_h(U_A) \int_0^{T_{p,\max}} g_1(T) dT \right] \right. \\
& \times \left[\int_{T_{tr}^{\min}}^{T_{tr}^{\max}} \frac{1 - \frac{eU_A}{T}}{2r_B^2 \sqrt{1 - \frac{1}{r_B} \left(1 - \frac{eU_A}{T}\right)}} g_2(T) dT \right] \\
& - \left[\int_{T_{tr}^{\min}}^{T_{tr}^{\max}} \left(1 - \sqrt{1 - \frac{B_0}{B_A} \left(1 - \frac{eU_A}{T}\right)}\right) g_2(T) dT + \int_{T_{tr}^{\max}}^{T_{p,\max}} g_2(T) dT - r_h(U_A) \int_0^{T_{p,\max}} g_2(T) dT \right] \\
& \left. \times \left[\int_{T_{tr}^{\min}}^{T_{tr}^{\max}} \frac{1 - \frac{eU_A}{T}}{2r_B^2 \sqrt{1 - \frac{1}{r_B} \left(1 - \frac{eU_A}{T}\right)}} g_1(T) dT \right] \right\} \\
& \times \frac{1}{\left[\int_{T_{tr}^{\min}}^{T_{tr}^{\max}} \left(1 - \sqrt{1 - \frac{B_0}{B_A} \left(1 - \frac{eU_A}{T}\right)}\right) g_2(T) dT + \int_{T_{tr}^{\max}}^{T_{p,\max}} g_2(T) dT - r_h(U_A) \int_0^{T_{p,\max}} g_2(T) dT \right]^2}
\end{aligned} \tag{2.20}$$

The relative uncertainty in a is plotted in Fig. 2.5. In order to reach the design goal of the spectrometer of 0.3 % in a , the relative uncertainty in r_B has to be kept below 1×10^{-4} .

For a special set of barrier voltages, $U_A = 50, 250, 400, 500, 600$ V, the relative change in a has been investigated for different uncertainties of the magnetic field ratio r_B [5] [22]. From Fig. 2.6, we derive an approximate relation between the relative uncertainties in r_B and a :

$$\frac{\Delta a}{a} \approx 10 \cdot \frac{\Delta r_B}{r_B} . \quad (2.21)$$

Since r_B is the ratio of B_A to B_0 , we need to investigate the influence of both fields on the ratio r_B . For this we use the Gaussian error propagation [29]:

$$\Delta f = \sqrt{\left(\frac{\partial f}{\partial x_1} \Delta x_1\right)^2 + \left(\frac{\partial f}{\partial x_2} \Delta x_2\right)^2 + \left(\frac{\partial f}{\partial x_3} \Delta x_3\right)^2 + \dots} . \quad (2.22)$$

and obtain

$$\Delta r_B = \sqrt{\left(\frac{\partial r_B}{\partial B_A} \Delta B_A\right)^2 + \left(\frac{\partial r_B}{\partial B_0} \Delta B_0\right)^2} = \sqrt{\frac{\Delta B_A^2}{B_0^2} + \frac{B_A^2}{B_0^4} \Delta B_0^2} \quad (2.23)$$

This formula can be expressed more elegantly:

$$\frac{\Delta r_B}{r_B} = \sqrt{\left(\frac{\Delta B_A}{B_A}\right)^2 + \left(\frac{\Delta B_0}{B_0}\right)^2} . \quad (2.24)$$

Figure 2.7 illustrates the relation between the relative uncertainty in the magnetic field ratio $\Delta r_B/r_B$ and the absolute uncertainties in the magnetic fields, ΔB_A and ΔB_0 , in a contour plot. In order to reach the design goal of a SPECT of 0.3 % in a , the relative error in r_B has to be kept below 1×10^{-4} . This is guaranteed in the dark blue area of Fig. 2.7. Hence, the absolute uncertainties of the magnetic field in the AP and in the DV need to be below about 1 and 5 Gauss, respectively.

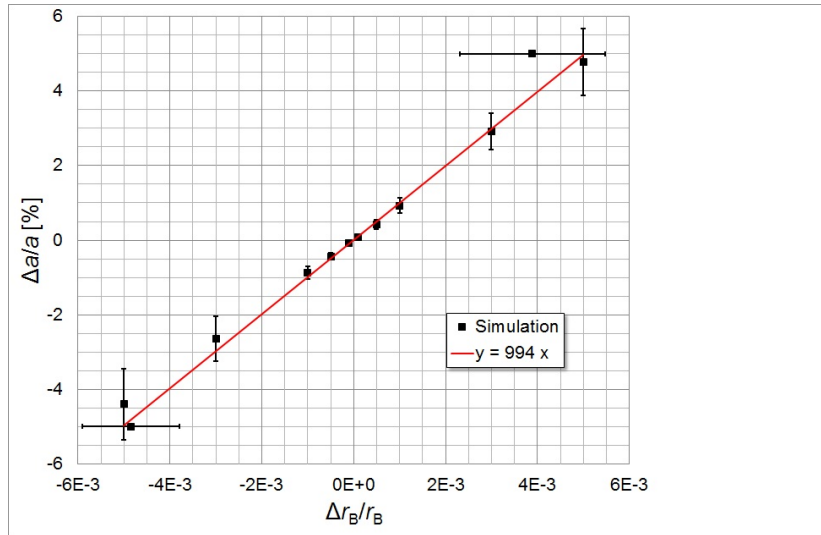


Figure 2.6: Relative uncertainty in a depending on the relative uncertainty in the magnetic field ratio r_B [5] [22]

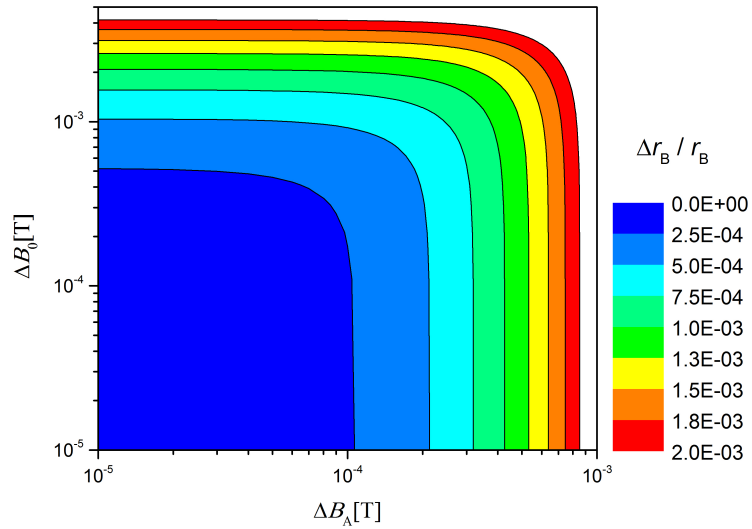


Figure 2.7: The relative uncertainty in the magnetic field ratio r_B depending on the absolute uncertainties in B_A and B_0 . (Input data: $B_A = 0.44$ T and $B_0 = 2.17$ T.)

Chapter 3

Improvement of the upper electrode system

During early beam times with the spectrometer *a*SPECT strong discharge phenomena at the detector electrode have been observed [6]. Those discharges not only made it impossible to reach the design goal of the *a*SPECT experiment, but also caused severe damages to several detectors. By improving the shape of the detector electrode [23] and changing the type of the detector [32], strong discharges could be suppressed. However, a strongly reduced background signal was still present [8]. This has been identified as positive ions from the residual gas [32]: Electrons emitted from the metal surfaces of the electrode system possess the capability to ionize atoms or molecules of the residual gas, which will then be accelerated on the detector and miss-counted like decay protons. Hence, further improvements in the electrode and in the vacuum system of the spectrometer have been inevitable.

This chapter deals with the optimization of the upper electrode system, including the detector electrode, and the investigation of the background during an off-line measurement in summer 2012 at the Institut Laue-Langevin (ILL) in Grenoble, France.

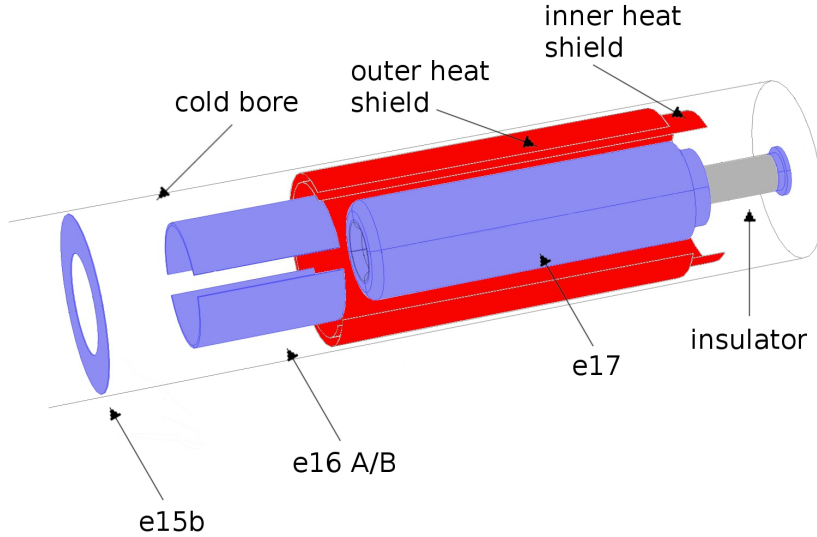


Figure 3.1: The upper electrode system of the *a*SPECT spectrometer. From left to right: the grounded top plate e15b of the lower electrode system (containing DV, AP lower $\vec{E} \times \vec{B}$ and the mirror electrode), both sides of the upper $\vec{E} \times \vec{B}$ dipole electrode e16A and e16B, respectively, the detector electrode e17 and the insulator, connected on top to the ground potential of the *a*SPECT magnet. The detector electrode is surrounded by two heat shields (red) to reduce the heat transfer to the cryostat. The large, transparent cylinder indicates the cold bore tube of the cryostat (which continues on the left and on the right side). Figure 3.7 shows the detector electrode e17 in more detail.

3.1 Motivation for a re-design of the upper electrode system

Main part of the upper electrode system¹, shown in Fig. 3.1, is the detector electrode. The detector electrode surrounds the proton detector and part of its electronics, and post-accelerates the decay protons onto the detector. For the currently used silicon drift detector (SDD), a potential of -15 kV has turned out to be a good compromise between signal-from-background separation and background

¹The indication 'upper' is based on the fact that the associated electrodes are inserted from the top of the *a*SPECT magnet, while the 'lower' (actual) electrode system is inserted from the bottom.

performance [32]. However, during the last beam time in summer 2011 at ILL, discharge phenomena have been observed again. In addition, all measurements (2005/06 at Forschungs-Neutronenquelle Heinz Maier-Leibnitz (FRM II) in Garching, Germany, and 2008 and 2011 at ILL) revealed an AP voltage dependent background, while the extraction of the electron-antineutrino correlation coefficient a from the measured proton recoil spectra assumes no dependency. The common position is that it is a result of Penning traps inside a SPECT.

After a brief description of the observed background behavior, I will give a short introduction to Penning traps and Penning discharges.

3.1.1 Background problems during earlier beam times

A fundamental prerequisite for the determination of the electron-antineutrino correlation coefficient a from the proton recoil spectra is that the background, measured at $U_A = 780$ V, is independent of the AP voltage. However, during the 2005/06 and 2008 beam times at FRM II and ILL, respectively, an AP voltage dependent background has been observed [6, 8, 27]. Figure 3.2 shows that for the 2008 beam time, the background and its AP voltage dependence have been effectively suppressed.

The common position is that the AP voltage dependence is the result of Penning traps (see Sect. 3.1.2 for details) inside the a SPECT spectrometer. Hence, an additional neutron shutter was installed several meters in front of the spectrometer to investigate the background count rates also without neutrons and, subsequently, without the charged neutron decay products. Figures 3.3 and 3.4 show examples of the temporal evolution of the background count rates during the 2008 and 2011 beam times, respectively. As can be seen from Fig. 3.3, in 2008, the background count rate could be strongly suppressed with reasonable settings of the lower $\vec{E} \times \vec{B}$ electrode e8 (cf. Fig. 3.6).

In 2011, this was not the case: Figure 3.4 shows a typical temporal evolution. For the background measurement with shutter closed (no neutrons), the AP voltage was ramped up to 780 V at $t = 10$ s and ramped down again to 0 V at $t = 175$ s. Before the AP is back again at 0 V, the background reaches a peak with a height of about 90 s^{-1} . After that, the background count rate drops back to its initial value

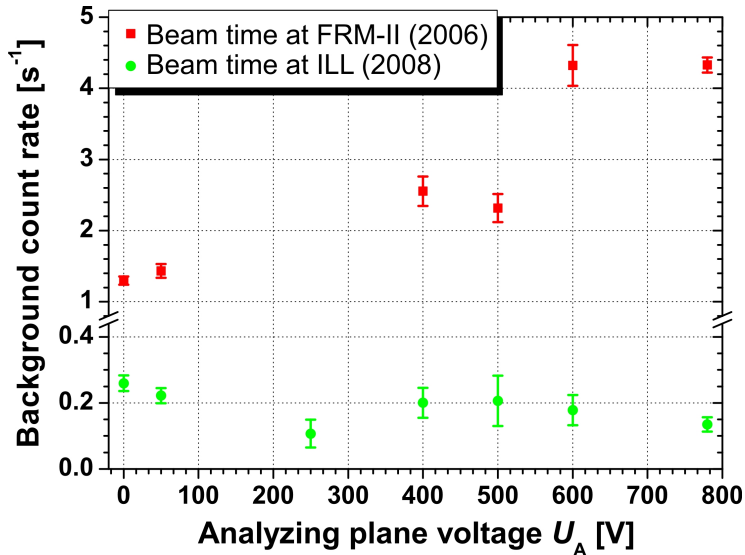


Figure 3.2: Background count rate without neutron beam depending on AP voltage, taken from [23]. The red squares stem from the worst data set of the 2006 beam time at FRM II, whereas the green circles stem from the 2008 beam time at ILL. See the text for details. Error bars show statistical errors only.

(sub-Hz). During measurements with neutrons, a similar AP voltage dependent peak appears. For this measurement the AP voltage was ramped up at $t=10$ s and ramped down again at $t=90$ s. The reason for the much higher and the much stronger AP voltage dependent background, compared to 2008, could not be clearly identified. The obvious suspicions are a too high gas pressure (see also Sect. 3.4) and the high-voltage electrodes.

To reach a relative accuracy in a below 0.1 %, the background count rate has to be known with a precision of 10 mHz [8, 23]. Hence, improvements of the a SPECT spectrometer for the recent beam time in summer 2013 were inevitable. The improvement of the high-voltage electrodes is discussed later in Sects. 3.2 and 3.3; the results of an off-line background measurement in summer 2012 are presented in Sect. 3.5.

For a more detailed background characterization of the beam times in 2008 and 2011 see Refs. [8, 23, 24].

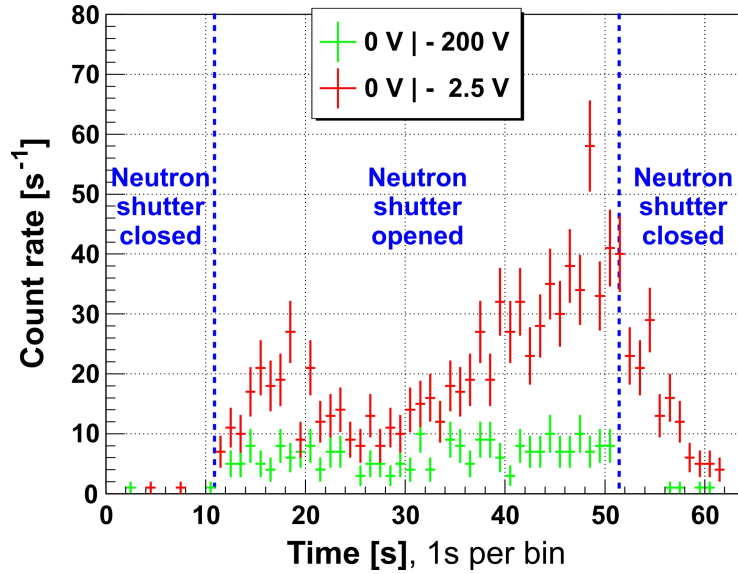


Figure 3.3: The temporal evolution of the background count rate measured at $U_A = 780$ V, for two different settings of the lower dipole electrode e8, during the 2008 beam time; taken from [23]. To illustrate, the dashed blue lines show when the neutron shutter was opened and later closed again. Error bars show statistical errors only.

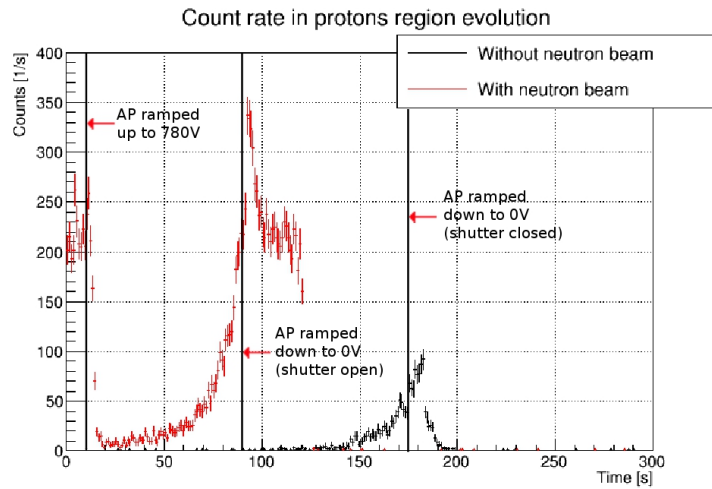


Figure 3.4: The temporal evolution of the background count rate measured at $U_A = 780$ V, with (red) and without (black) neutrons. The figure shows a typical example of the 2011 beam time at ILL [25]. See the text for details. Error bars show statistical errors only.

3.1.2 Penning traps and Penning discharges

This chapter is basically following the presentation of F. Glück [16]. Most discharge phenomena are explained by ionization processes through electrons. The source for ionizing electrons may however vary. An unintended source for electrons are metal surfaces, where electrons can tunnel through the potential barrier. Such electrons do not have sufficient kinetic energy to ionize atoms or molecules of the residual gas. Hence, ionization will occur, only if the electrons are accelerated by an electric field. When electrons, which have gained the ionization energy, collide with neutral atoms or molecules of the residual gas, not only ions will be produced but also secondary electrons. In this way, an electron avalanche will be triggered. The ion cloud between two electrodes can then reduce the resistance of the residual gas and discharge phenomena will occur. Additionally to electron field emission, secondary electron emission from the metal surface through cosmic rays and gammas cannot be excluded. The crucial factors that influence the probability for discharges are the mean free path of the electrons within the residual gas and the distance between anode and cathode. At low gas pressure and small distance between the electrodes, the electrons will not collide with residual gas atoms or molecules and ionization and consequently discharges will not be initiated. This simple mechanism of discharge occurs only at bad vacuum conditions and is known as Townsend discharge.

Discharge processes in *a*SPECT cannot be explained by the Townsend discharge as the gas pressure is too low ($<10^{-8}$ mbar) and therefore the mean free path of the electrons is too long. In *a*SPECT, the so called Penning discharge is responsible for discharge phenomena. Additionally to the electric field, we have a strong magnetic field inside the *a*SPECT spectrometer. As discussed in Sect. 2.1 charged particles gyrate around magnetic field lines. If the magnetic and the electric field are arranged in the right direction, charged particles can be stored. This kind of particle trap is known as Penning trap. Figure 3.5 shows typical a Penning trap. If the magnetic field lines connect the anode and the cathode, no storage of particles is possible as the electrons or ions will impact on one of the electrodes without increasing the duration of stay within the residual gas. In this case, the electric and the magnetic field lines are parallel. However, if a magnetic field line connects two parts of

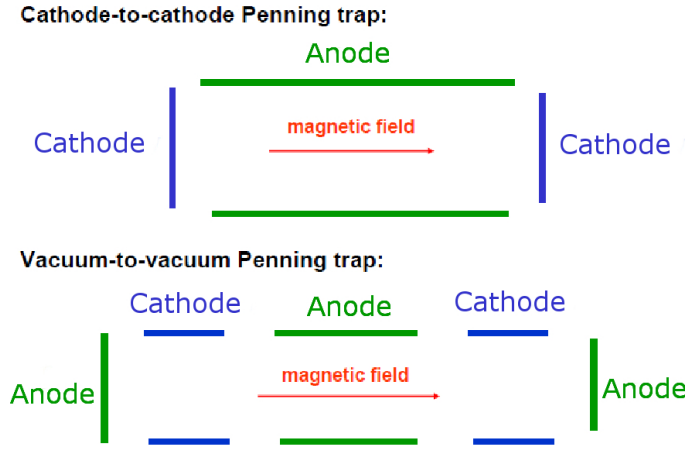


Figure 3.5: Typical arrangement of Penning traps, taken from [16]. The sketch shows a cathode-to-cathode Penning trap (upper part) and a vacuum-to-vacuum Penning trap (lower part).

a cathode or two different cathodes and the potential in between is more positive, because of an anode, charged particles can be stored and even accelerated [16]. As the time spent in the traps and the kinetic energy of electrons can be increased in Penning traps, the probability for ionization and subsequently discharges increases and therefore occurs even in good vacuum conditions.

Penning traps are not necessarily identical to the ones shown in Fig. 3.5. Great effort has been invested to identify and subsequently eliminate Penning traps inside *a*SPECT. Figure 3.6 indicates those Penning traps that have been identified after the first measurements with *a*SPECT at FRM-II, cf. Ref. [6]. For the 2008 beam time, the Penning traps at the electrostatic mirror (e1) and at the upper $\vec{E} \times \vec{B}$ electrode (e16) have already been eliminated. Though it would be desirable to remove all Penning traps in *a*SPECT, it is not possible as some are required for the operation of a retardation spectrometer, like in the AP.

Since some Penning traps cannot be removed, the probability for field emission from the electrodes' surfaces must be suppressed to a minimum. Field emission usually occurs at electric fields above 1 GV/m [16]. In *a*SPECT, the maximum electric field appears at the

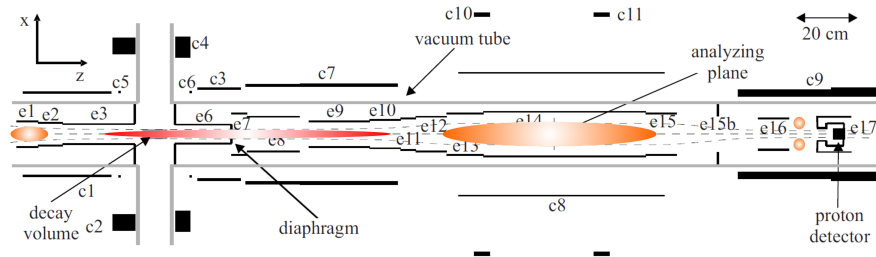


Figure 3.6: Sketch of the *a*SPECT experiment: Penning traps for electrons (orange) and for positive ions (red), taken from [23]. The traps at e1 and e16 have already been removed [23].

surface of the detector electrode, but does not exceed some MV/m. However, simulations of the electric field assume perfectly smooth surfaces. Furthermore, simulations of sharp edges and small radii with the finite element method are always limited by the minimum size of mesh elements. Assuming that any surface is a structure containing of separated tiny peaks, which generate much higher electric fields, field emission cannot be excluded. Therefore the surface of the (high-voltage) detector electrode is electro-polished.

Scratches that can easily be caused during mounting or transport can result in discharge phenomena. Therefore a second detector electrode should always be available during a beam time, as a spare part. For the 2013 beam time, we have decided to build an improved version of the detector electrode. As motivated above, the design of the electrode was changed in order to reduce field emission. The changes are summarized in the following Sect. 3.2.

3.2 Re-design of the detector electrode

The motivation for a re-design of the detector electrode e17 (cf. Fig. 3.1) has been given in Sect. 3.1. This electrode post-accelerates all decay protons which overcome the potential barrier in the analyzing plane onto the proton detector. For this, a negative potential of -15 kV is applied. Figure 3.7 shows the set-up currently used, including the detector and its electronics as well as the insulator which separates the high-voltage side of the detector from the ground potential side of the *a*SPECT magnet. The electrode itself consists of

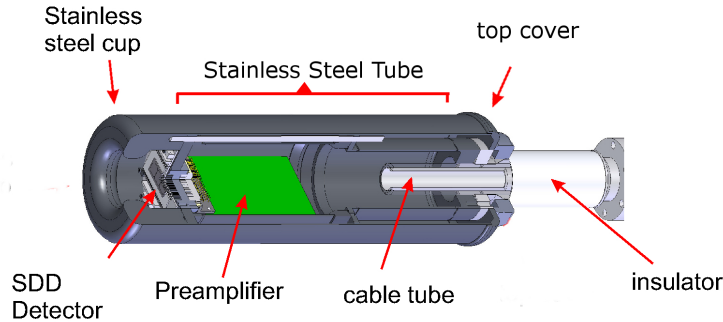


Figure 3.7: Sketch of the detector electrode e17; adapted from [32]. The electrode consists of three main parts, from left to right: the detector cup, a stainless steel tube and the top cover. For details see the text.

three main parts: the detector cup, an approximately 35 cm long tube containing parts of the electronics, and (the parts of) the top cover. The detector cup is a solid stainless steel part. Its purpose, besides the shaping of the electric field, is the radiative shielding of the detector, mainly from gammas. The stainless steel tube attached to it contains the preamplifier of the detector. As shown later in Fig. 3.14 the cup and the tube are mounted via a cylindrical, hollow insulator. The top cover parts of the electrode cover the sharp-edged welding seam of the insulator as well as the connection screws. For upcoming beam times, an improved version of the detector electrode has been built, which also serves as a spare part for the current electrode. In particular, the use of two different electrodes is very useful to test the stability and the reproducibility of the background. In this section the improvements on the shape of the detector electrode are presented.

3.2.1 Re-design of the detector cup

The detector cup surrounds the proton detector and shields it from radiation. Main part of the radiation are gammas which are generated by neutrons, cosmic rays or neighboring experiments. The detector cup as part of the detector electrodes e17 is held at a potential of -15kV. As shown in Fig. 3.1, the detector electrode is surrounded by grounded heat shields to minimize the heat input from the detector electrode to the cold bore tube of the *a*SPECT magnet. In the direction of the AP the dipole electrode e16 is mounted which ad-

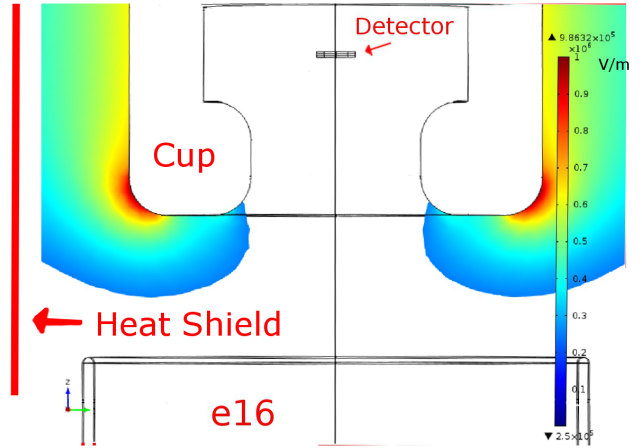


Figure 3.8: Electric field of the detector cup currently used in a z - y plane at $x=0$: The cup has a cylindrical shape with rounded edges on the inner and the outer sides. Here the rounding has a radius of 1 cm. In the red areas the simulation yields an electric field of up to 1×10^6 V/m. Input data: $U_{16A} = -4200$ V, $U_{16B} = -200$ V and $U_{17} = -15$ kV.

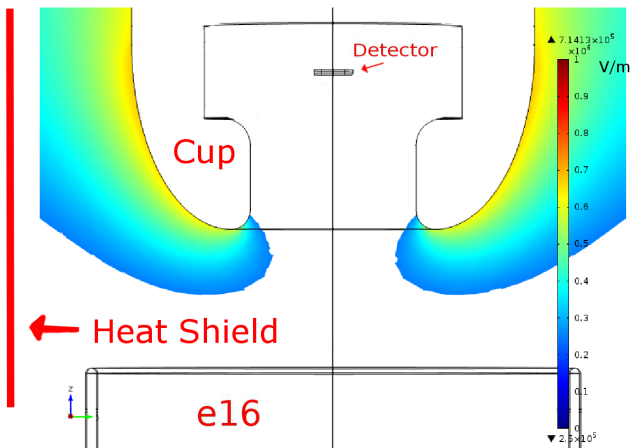


Figure 3.9: Electric field of the re-designed detector cup in a z - y plane at $x=0$: The outer side of the cup has an elliptical shape. This way, the electric field has been reduced significantly. Compared to Fig. 3.8 no red areas are present. Input data: $U_{16A} = -4200$ V, $U_{16B} = -200$ V and $U_{17} = -15$ kV.



Figure 3.10: Photographs of the re-designed detector cup.

justs the neutron (proton) beam on the detector. Typical values for the potentials are -4200 V and -200 V for side A and B, respectively. The small distances to the heat shields cause strong gradients of the electrostatic potential. Hence, a strong electric fields emerges at the surface of the detector cup as can be seen from Fig. 3.8.

To minimize the probability for field emission from the detector cup, the electric field should be as small as possible. But the changes that can be made to the cup are strongly limited. On the one hand, the radial distance to the heat shields and to the electrode e16 should not be further reduced. On the other hand, the tube containing the preamplifier should be as light as possible and compatible with the insulator and parts of the detector electronics. Hence, the dimensions of the tube have not been changed. Since the connection between the tube and the cup has to be smooth, the outer diameter of the cup at the transition is fixed. The rest of the cup could be changed.

The optimization of the detector cup has been performed with COMSOL Multiphysics 4.2a [10], a finite element analyzing software package. A variety of shapes has been simulated in order to find the best solution. The final shape is shown in Fig. 3.9. An elliptical shape on the outer side of the cup yields the best result. A simple explanation for this effect is the small curvature of the cup close to the grounded heat shields. The comparison between Fig. 3.8 and Fig. 3.9 shows that red areas, which mark electric fields between 8×10^5 and 1×10^6 V/m, are no longer present on the surface of the re-designed cup. The simulated maximum of the electric field has

been reduced by almost 30 %. Figure 3.10 shows photographs of the re-designed detector cup.

3.2.2 Re-design of the top cover

The detector electrode e17 is mounted on the detector mechanics (see later in Fig. 3.14) via an insulator, see Fig. 3.7. The flange of the insulator on the electrode side and therefore the connection screws are on the electrode potential of -15 kV. In order to suppress field emission, the sharp-edged welding seam of the flange as well as the upper end of the electrode tube must be covered. The parts fulfilling this purpose are referred to as the top cover of the detector electrode e17.

The current top cover shown in Fig. 3.11 (left) consists of three parts: one large ring, which is simply put over the end of the electrode tube, and two half rings, which cover the welding seam. Before mounting the detector electrode on the insulator, the large ring must be put over the insulator, since it does not fit over the detector cup and cannot be mounted afterwards. Necessarily the inner diameter of this ring is bigger than the outer diameter of the insulator flange. After mounting the electrode the remaining half rings are placed on top of the larger ring and cover the welding seam and the connection screws of the insulator. A slit between the two half rings is inevitable. In the current design this slit is not covered and points to the heat shields. In contrast, the re-designed top cover shown in Fig. 3.11 (right) not only yields a significantly lower electric field but also has no slit pointing to the direction of the heat shields. The assembly works totally analogous. However, the small ring (consisting of two half rings) is pushed inside the larger ring.

The electric fields of both top covers are shown in Fig. 3.12. The higher field of the current top cover is concentrated in two areas (one on each of the two rings) and has a maximum above 1×10^6 V/m. The re-designed top cover is surrounded by a larger area in which the field varies between 0.7 and 0.8×10^6 V/m (yellow and orange area), but does not exceed this value. For these simulations the slits in the smaller ring of the old top cover have been neglected. Even taking into account the slits for the new top cover, the maximum electric field has been reduced by about 20 %. Figure 3.13 shows photographs of the re-designed top cover.

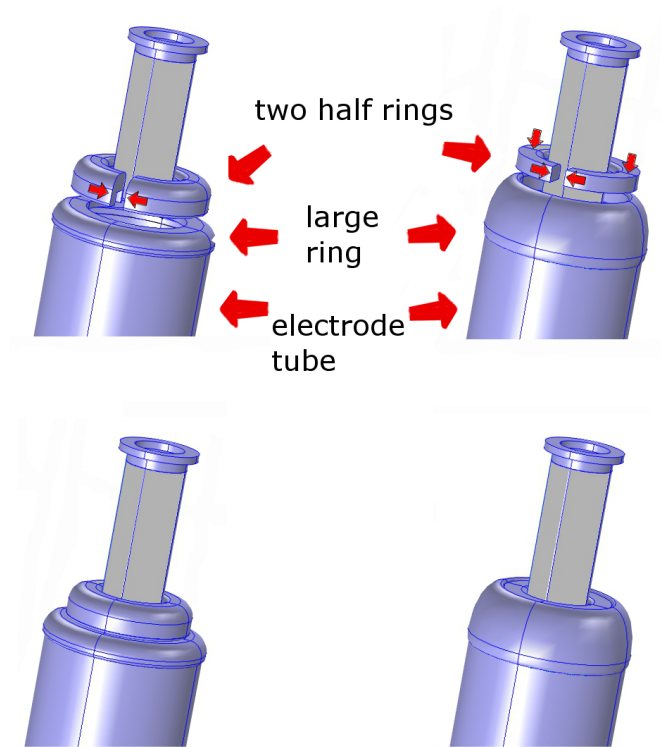


Figure 3.11: Illustration of the assembly of the old (left) and of the new (right) top cover. The large ring covers the end of the tube, the two half-rings the welding seam and the connection screws of the insulator.

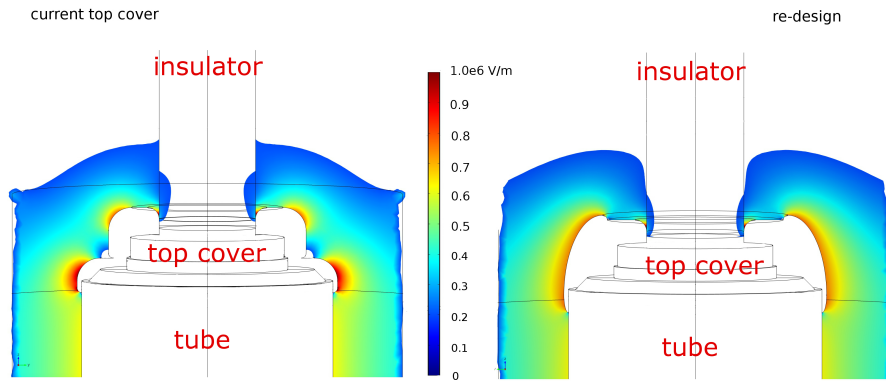


Figure 3.12: Electric field of the old (left) and of the new (right) top cover. The maximum electric field has been reduced by about 30 %. The old top cover has two areas of high electric field (at each ring), the new top cover has a larger orange area of a reduced electric field. Input data: $U_{17} = -15$ kV.



Figure 3.13: Photographs of the re-designed top cover of the electrode e17: left and middle: outer ring, right: two half rings which are pushed inside the outer ring.

3.2.3 Influence of the position on the electric field

The detector electrode e17 is mounted on a membrane bellow, in order to make it retractable in the z -direction. The reason for this is the following: During earlier beam times with *a*SPECT problems with the detector occurred now and then. In order to save time, the detector should therefore be accessible without venting the whole vacuum system. A sketch of the so-called detector mechanics is shown in Fig. 3.14. For the removal, the electrode is pulled up above an ultra-high vacuum (UHV) shutter. Then the shutter is closed and the electrode can be removed without breaking the UHV in the cold bore tube. In the measurement position the distance from the lower end of the electrode e17 (the detector cup) to the suspension point is approximately 1.5 m. Consequently the x - y centering of the detector electrode is not perfectly guaranteed, due to the tolerances of the mounting system. The influence of an x - y displacement of the detector cup on the electric field is investigated in this section.

Figures 3.15 and 3.16 show the dependence of the maximum electric field on a displacement in the x - and in the y - direction, respectively. For each direction a maximum displacement of the detector cup of 1 cm has been assumed. The electric field increases rather linear with the displacement. At the maximum displacement of 1 cm, the electric field has increased by about 20 %. For a displacement in the y -direction the electric field increases to a higher level. The reason for this is the opening angle of the dipole electrode. At a displacement of about 1 cm the electric field of the new detector cup reaches the electric field of the old detector cup, in center position. For x - and y - direction, the difference between the old and the new cup stays rather constant. The slight asymmetry between the negative and the positive displacement in the x -direction (Fig. 3.15) is most likely caused by the upper $\vec{E} \times \vec{B}$ electrode, in the asymmetric standard configuration ($U_{16A} = -4200$ V and $U_{16B} = -200$ V)². Simulations of the electric field for the old and the new detector cup in the center position and at the maximum displacements of $x=-1$ cm and $y=1$ cm are shown in Figs. 3.17 and 3.18.

Nevertheless, the maximum electric field of the old detector cup in

²The different values for the electric field in the center position as well as the anomalies in Fig. 3.15 can be explained by the quality of the simulations (error of about $2 \cdot 3 \cdot 10^{-4}$)

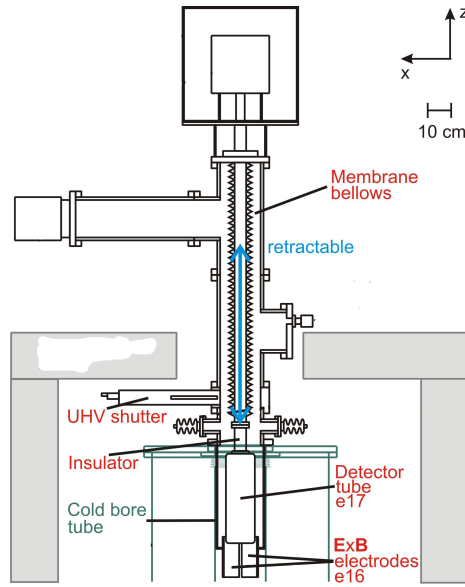


Figure 3.14: Sketch of the detector mechanics, taken from [23]: the detector electrode e17 can be removed from the spectrometer without breaking the main vacuum. For this purpose the electrode is mounted on a membrane bellows. After pulling up the electrode the UHV shutter is closed. In the measurement position, the distance from the lower end of the electrode e17 (the detector cup) to the suspension point is about 1.5 m. Therefore the perfect x - y -centering is not guaranteed.

the center position is higher than the maximum electric field of the new detector cup displaced by 1 *cm* in the x - or y -direction.

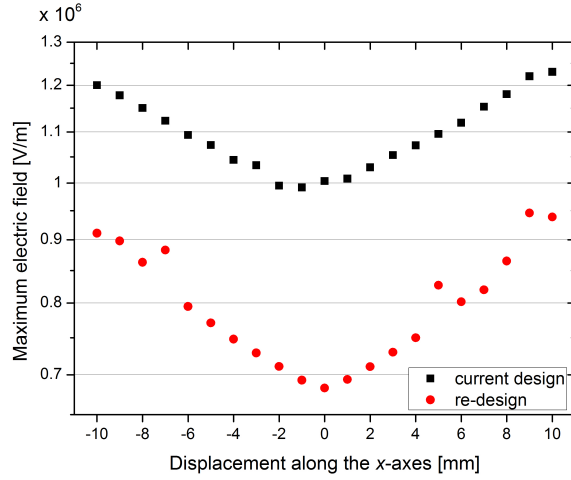


Figure 3.15: Maximum electric field at the surface of the detector electrode as a function of the displacement in the x -direction. Input data: $U_{16A} = -4200$ V, $U_{16B} = -200$ V and $U_{17} = -15$ kV.

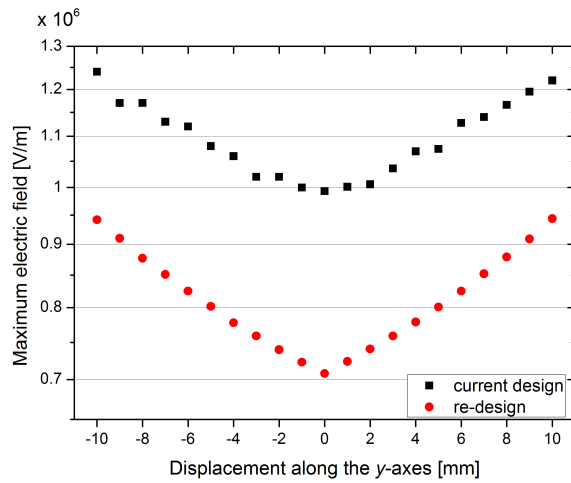


Figure 3.16: Maximum electric field at the surface of the detector electrode as a function of the displacement in the y -direction. Input data: $U_{16A} = -4200$ V, $U_{16B} = -200$ V and $U_{17} = -15$ kV.

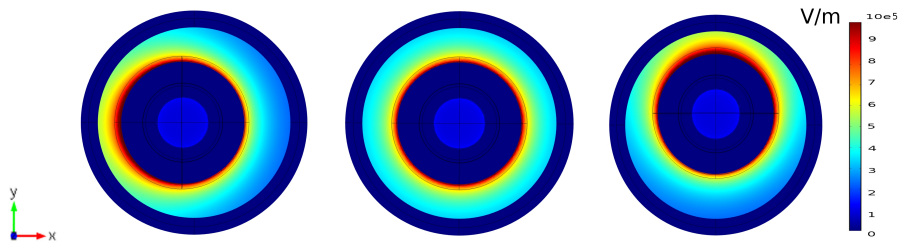


Figure 3.17: Electric field of the current detector cup in the x - y plane with the highest field value (at $z = 2.18$ m). From left to right, for a displacement of 10 mm in the negative x -direction, for the center position and for a displacement of 10 mm in the positive y -direction. Input data: $U_{16A} = -4200$ V, $U_{16B} = -200$ V and $U_{17} = -15$ kV.

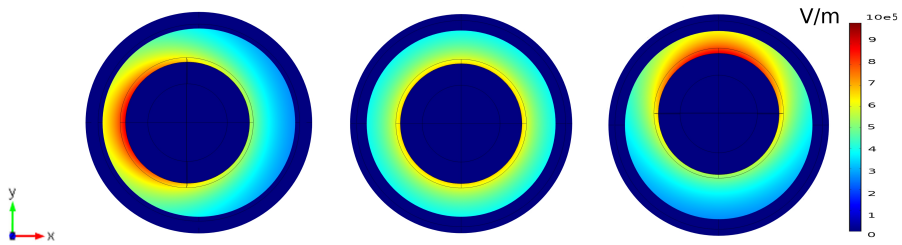


Figure 3.18: Electric field of the re-designed detector cup in the x - y plane with the highest field value (at $z = 2.22$ m). From left to right, for a displacement of 10 mm in the negative x -direction, for the center position and for a displacement of 10 mm in the positive y -direction. Input data: $U_{16A} = -4200$ V, $U_{16B} = -200$ V and $U_{17} = -15$ kV.

3.3 Improvement and repair of the upper $\vec{E} \times \vec{B}$ electrode

The purpose of the upper $\vec{E} \times \vec{B}$ electrode is the adjustment of the neutron (proton) beam on the detector. Its position can be seen in Fig. 3.1. The dipole electrode consists of two half cylinders to which different potentials can be applied. To further investigate the probability for field emission from this electrode, simulations of the electric field for 'different shapes' of the electrode have been performed, which are presented in Sect. 3.3.1.

An offline-measurement in summer 2012 at ILL has been dedicated to the study of the spectrometer background. Unfortunately, it turned out that a glass insulation was broken and subsequently had to be repaired. An epoxy resin with insufficiently known UHV performance has been used. To ensure best possible UHV conditions for the background measurements (see also Sect. 3.4) a test pumping station with the option of baking out has been built. The results of the vacuum tests are also discussed in this chapter.

3.3.1 Investigation of the electric field at the edges

In order to get an impression of the electric field at the upper $\vec{E} \times \vec{B}$ electrode e16, further simulations with COMSOL Multiphysics 4.2a [10] have been performed. For this, the standard configuration of $U_{16A} = -4200$ V and $U_{16B} = -200$ V has been assumed. As expected, the maximum electric field occurs at the edges of the electrode side to which the higher potential of -4200 V is applied.

The electrode has been built from stainless steel sheet, with sharp edges. Subsequently the sharp edges have been removed/rounded. The exact radius of curvature is unknown. Thus, Fig. 3.19 shows a simulation for a rather small curvature, while Fig. 3.20 shows one for a diameter over the whole thickness of the electrode. For both shapes, the maximum electric field is almost the same. The actual shape might be somewhere in between and hence the maximum electric field also the same. Compared with the detector electrode, the maximum electric field is about half a magnitude smaller at the edges of the upper $\vec{E} \times \vec{B}$ electrode.

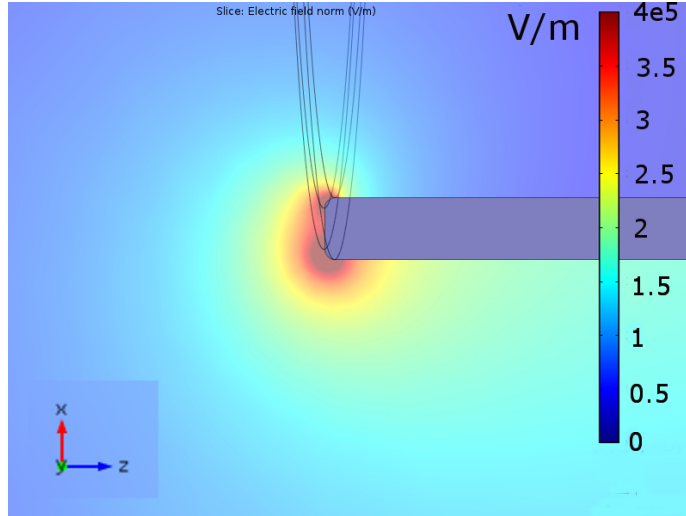


Figure 3.19: Electric field at one edge of the upper $\vec{E} \times \vec{B}$ electrode e16 in the x - z plane at $y = 0$: edge rounded with a rather small radius. Input data: $U_{16A} = -4200$ V, $U_{16B} = -200$ V and $U_{17} = -15$ kV.

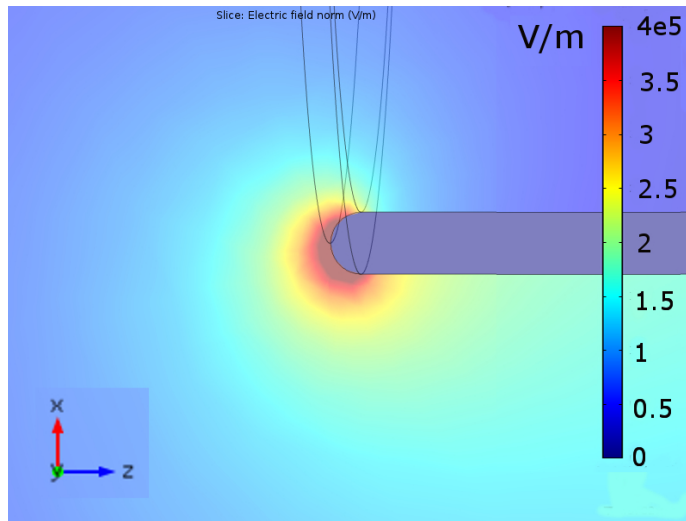


Figure 3.20: Electric field at one edge of the upper $\vec{E} \times \vec{B}$ electrode e16 in the x - z plane at $y = 0$: edge rounded with the radius half of the electrode thickness. Input data: $U_{16A} = -4200$ V, $U_{16B} = -200$ V and $U_{17} = -15$ kV.

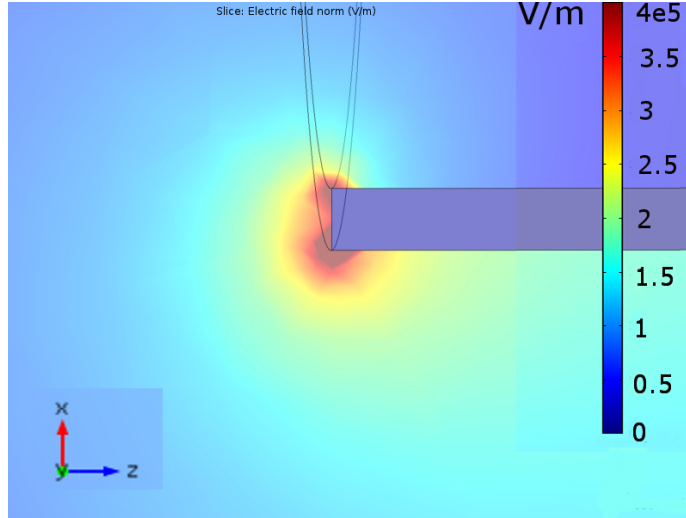


Figure 3.21: Electric field at one edge of the upper $\vec{E} \times \vec{B}$ electrode e16 in the x - z plane at $y = 0$: sharp edge, no curvature. Input data: $U_{16A} = -4200$ V, $U_{16B} = -200$ V and $U_{17} = -15$ kV.

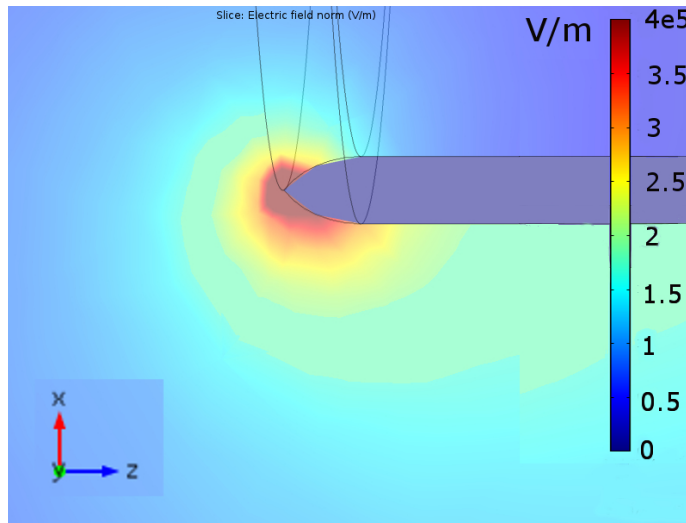


Figure 3.22: Electric field at one edge of the upper $\vec{E} \times \vec{B}$ electrode e16 in the x - z plane at $y = 0$: sharp edge, curvature that could appear when badly manufactured. Input data: $U_{16A} = -4200$ V, $U_{16B} = -200$ V and $U_{17} = -15$ kV.

To see whether sharp edges can have an extreme influence on the electric field, further shapes have been simulated, see Figs. 3.21 and 3.22. Keeping the same mesh size, no field increase could be observed. Please note that any sharp edge is limited by the minimum size of mesh elements.

Finally, we conclude that the electric field at the upper $\vec{E} \times \vec{B}$ electrode e16 is approximately half of that at the detector electrode e17. However, sharp edges may cause unexpected high fields. But, as long as a smooth curvature is guaranteed, a re-design of the upper $\vec{E} \times \vec{B}$ electrode is not necessary; with respect to the magnitude of the electric field.

3.3.2 Outgassing tests for STYCAST 2850 FT with catalyst 9

The connection cables of the upper $\vec{E} \times \vec{B}$ electrode are isolated through glass tubes, cf. Fig. 3.23. During the assembly of the *a*SPECT spectrometer for an off-line measurement at the ILL, in summer 2012, it turned out that a glass insulation was broken close to the electrode. For lack of a new glass tube, it was decided to repair the glass with an epoxy resin (STYCAST 2850 FT with catalyst 9). Since no sufficient information about the UHV performance of the epoxy resin was available, it was decided to build up a CF-test pumping station³. This is to ensure best possible UHV conditions for the background measurements (see also Sect. 3.4) The repaired electrode was mounted inside a CF200-tube. On one end of the tube, a rather powerful turbo-molecular pump was mounted. On the other end, a mass spectrometer (Pfeiffer PrismaPlusTM QMG 220F) was installed, in order to analyze the residual gas composition inside the test chamber. The vacuum pressure was monitored with a full range vacuum gauge (Pfeiffer PKR 261). In order to reach good vacuum conditions it is a common procedure to increase the temperature within the vacuum system. This procedure is known as bake-out and accelerates the outgassing from surfaces. For the bake-out, we used heating tapes, wrapped around the test chamber, and isolated the whole set-up through aluminium foil.

³CF systems use only copper gaskets and therefore better vacuum conditions can be achieved than with KF systems, which use rubber gaskets

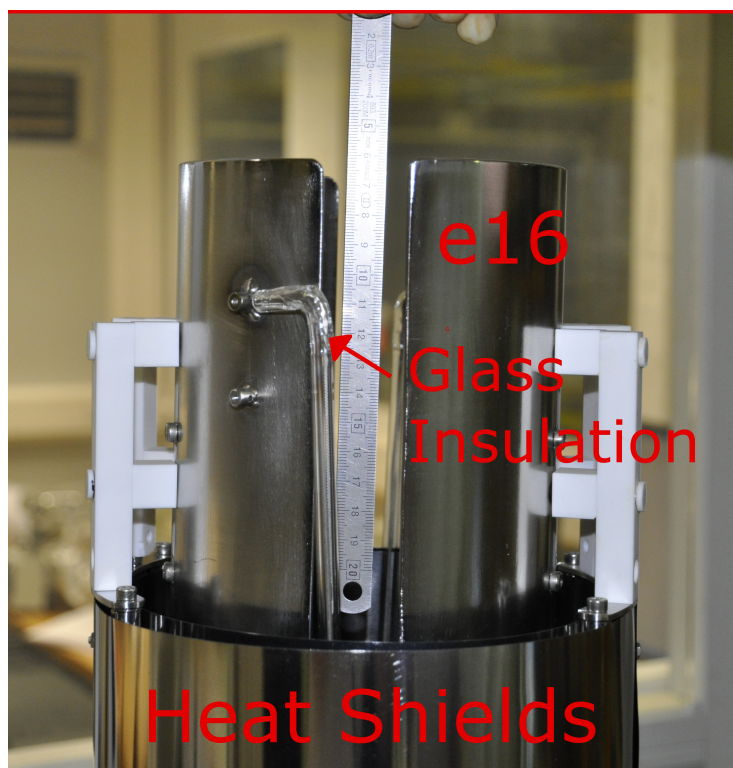


Figure 3.23: Photograph of the upper $\vec{E} \times \vec{B}$ electrode: The glass insulation of the connection cables easily breaks at the elbow, close to the electrode.

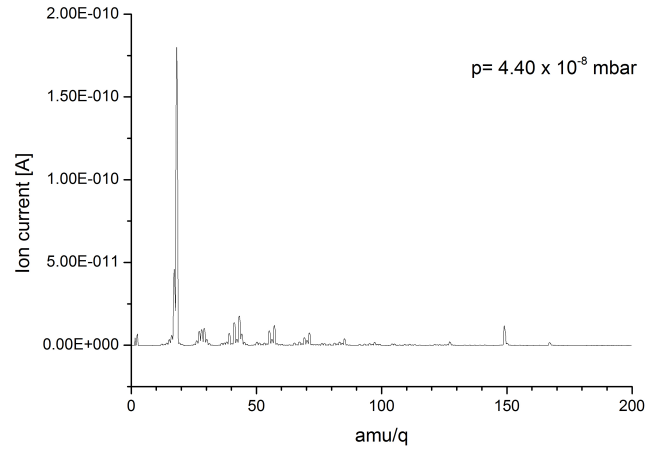


Figure 3.24: Mass spectrum taken before the start of the bake-out of the test chamber containing the repaired $\vec{E} \times \vec{B}$ electrode. The dominant peak at amu 18 is the main peak of water. For further details see Figs. 3.25 and 3.26.

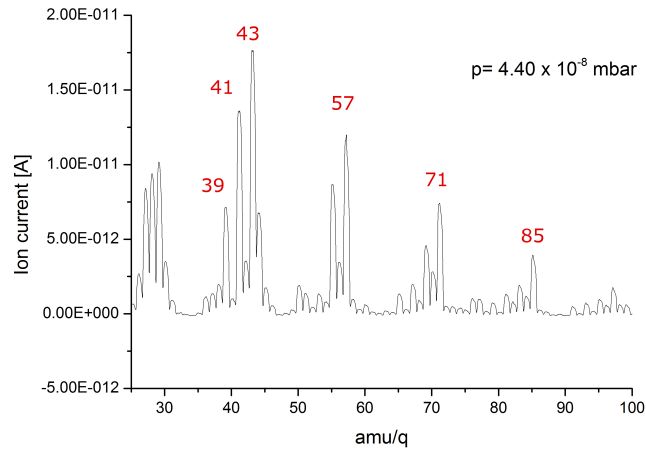


Figure 3.25: Zoom of Fig. .3.24, to mass number 25-100: The peaks at amu 39, 41, 43, 55 and 57 are most likely remnants of pumping oil. This is confirmed by peaks at amu 71 and 85 [14].

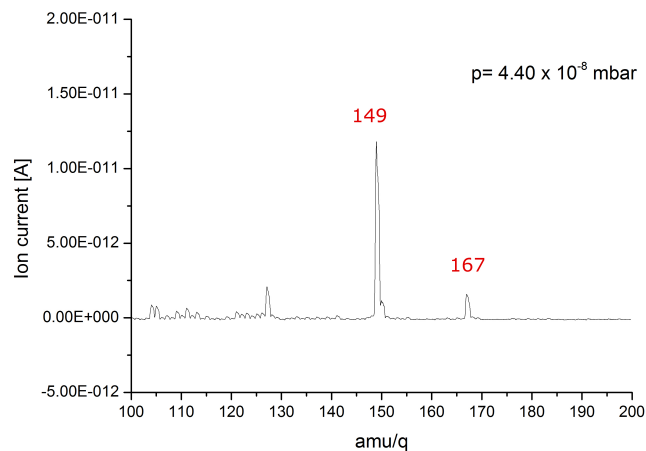


Figure 3.26: Zoom of Fig. 3.24, to mass number 100-200: The peaks at amu 149 and 167 are the main peaks in the mass spectrum of diethylhexylphthalate [13], a commonly used plasticiser, which is most likely be a part of the epoxy resin.

During the bake-out mass spectra have been taken and analyzed offline. A mass spectrum recorded before the start of the bake-out is shown in Figs. 3.24, 3.25 and 3.26. The high peak at mass number (m) 18^4 indicates that water is dominant in the chamber. Literature research and comparison of typical ingredients of epoxy resins with the dominant peaks at higher mass numbers (between $m=25$ and 100) did not show a high level of agreement. Most likely those peaks are caused by remnants of pumping oils [14] as confirmed by the peaks at $m=39, 41, 43, 55$ and 57 [14]. This hypothesis is further confirmed by other peaks at $m=71$ and 85 with a distance of 14 amu, what is also typical for pumping oils and lubricants [14]. Though the turbo pump used should be oil-free, earlier careless use may have caused some pollution. However, this assumption should not be over-estimated as the ionization probability for hydrocarbons is rather high, compared to, e.g., water [14]. The only peaks which can be associated with the epoxy resin are the peaks at $m=149$ and 167. These peaks are the largest peaks of diethylhexylphthalate [13] which is a commonly used plasticiser. To make absolutely

⁴The term mass number is not perfectly correct, since the mass spectrometer measures the ratio of mass to charge.

sure diethylhexylphthalate is a part of the epoxy resin, a reference measurement before the repair of the glass insulation would have been necessary. On the other hand, Figs. 3.27 and 3.28 show one of the last mass spectra taken. It contains the typical peaks one expects for water: 1 (H+), 2 (H₂⁺/H⁺⁺), 16 (O+), 17 (OH+) and 18 (H₂O). Furthermore, the small peak at m=28 is associated with molecular nitrogen (N₂). Here, we exclude carbon monoxide (CO), as it is not only gives a peak at m=28, but also at m=14 (C) and m=44 (CO₂). Hydrogen (water) is hard to pump and is expected to be the last molecule still present in UHV. The same accounts for the noble gas nitrogen. An air leak can not be excluded, because of the peak at m=16 (O+), while the typical peaks at m=14 (N) and m=32 (O₂) are missing.

The dominant peaks of water, pumping oils and the plasticiser were subjected to detailed analysis. The height of the peaks at m= 18, 43 and 149 has been extracted from the mass spectra in order to investigate the associated concentrations over time throughout the bake-out. Since no mass spectra were taken during the night, the data are incomplete. For this reason, the results of the detailed analysis are summarized quantitatively: The height of all of the three peaks increases with rising temperature. After two hours of heating, a temperature of about 80 °C has been reached⁵. At this point, the associated ion current of all three mass numbers starts to decrease, even though the temperature further increases up to about 100 °C. The temperature has been kept constant at this level over the night. In the morning after about 20 hours of heating, the peaks at m= 43 and 163 cannot be discriminated from the background any more. At this point, an electric breakdown paused the heating. During the 'unplanned second' bake-out a similar increase of concentration with temperature has been observed for the peaks at m= 18 and 43, however, at a significantly lower level. The peak at m=149, associated with a plasticiser, has not been observed any more.

The test station was pumping for approximately two days. A final pressure of less than 5×10^{-9} mbar (lower limit of the vacuum gauge) was achieved. The final pressure and the final mass spec-

⁵We note that the temperature has been measured on the outer surface of the CF-tube. The temperature inside the test chamber is not necessarily the same.

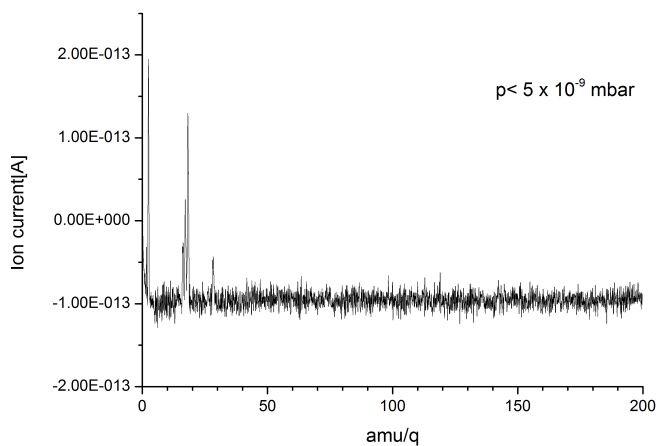


Figure 3.27: Mass spectrum after two and a half days of pumping and one and a half day of bake-out. Compared to Fig. 3.24, the maximum ion current decreased by about three orders of magnitude and the plasticiser and the pumping oils have vanished.

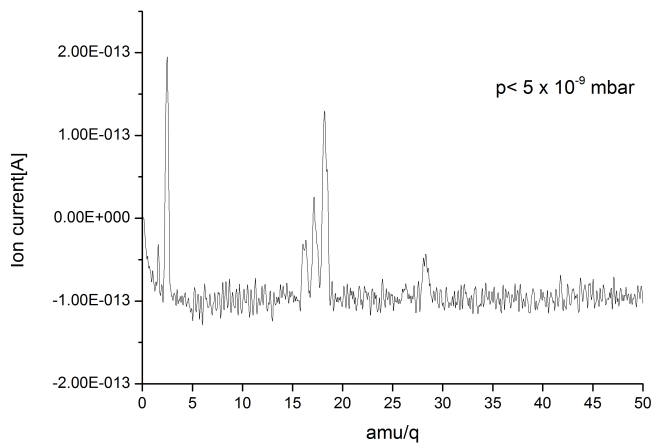


Figure 3.28: Zoom of Fig. 3.27 to mass number 0 to 50. In the mass spectrum no remnants of pumping oils (at mass numbers 39, 41 and 43 are visible).

tra indicate that the epoxy resin used is appropriate for the use in UHV systems (at least after moderate bake-out). Furthermore, the outgassing tests confirmed that the repair of the glass insulation did not endanger the background measurements envisaged (for details see Sect. 3.4 and [24]).

During the off-line measurements in 2012 there have been no alternatives to the repair of the glass insulation. Hence, the outgassing tests were mandatory. For the beam time in summer 2013, the stainless steel connection cable and the glass insulation have been exchanged by Kapton-insulated wires.

3.4 Discharge tests at worsened vacuum conditions

As mentioned above, in summer 2012 off-line background measurements with the spectrometer *a*SPECT have been performed at ILL. The whole spectrometer has been assembled in the configuration which has been used during the beam time in 2013. The purpose of these off-line measurements was to find out whether further improvements of the spectrometer yielded the expected results: further decrease of the background signal observed in earlier beam times [6], [8] and elimination of the reasons for the dramatically increased background count rate during the 2011 beam time [24]. On the one hand, some changes have been applied to the electrode system, compared to the beam time in 2011. On the other hand, the vacuum system has been improved by adding additional turbo molecular pumps (cascaded) and replacing the internal non-evaporable getter pumps (SAES C400 DSK cartridges) close to the analyzing plane/lower $\vec{E} \times \vec{B}$ and the mirror electrode. We note that the collimation system and the online NMR magnetometer have not been installed.

As soon as good UHV conditions ($p \approx 2 \times 10^{-9}$ mbar) have been established, we started with the background measurements. For the first tests, the detector has not been installed in order to prevent its destruction, which could be caused by unexpected discharges. By applying specific potentials at the upper $\vec{E} \times \vec{B}$ electrode and

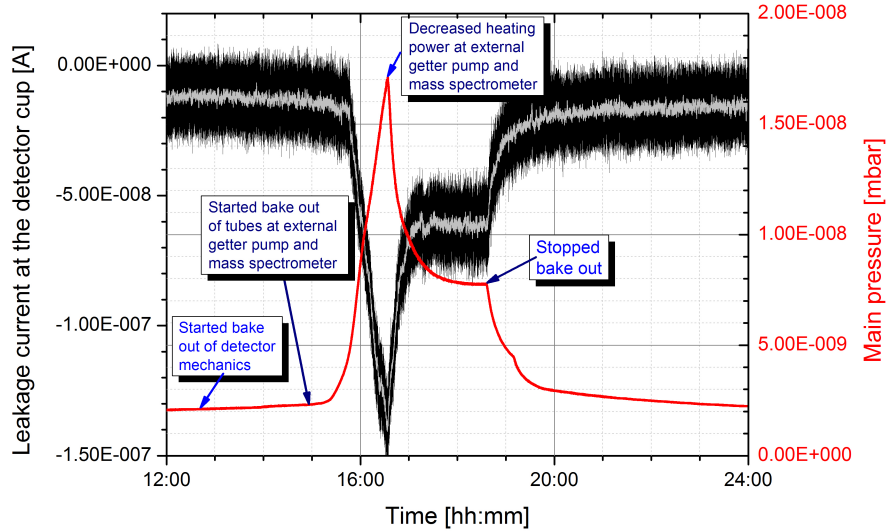


Figure 3.29: Behaviour of main pressure and leakage current at the detector electrode during the bake-out of the spectrometer *a*SPECT. A correlation is evident.

different voltages at the analyzing plane electrode, we tried to provoke discharges at the detector electrode. But, no discharges have been observed. The leakage current at the detector electrode stayed constant for all voltage settings.

In order to see, if discharges could be initiated at higher pressure, we started to increase the temperature within the spectrometer by wrapping heating tapes around various side ports. Since the superconducting coils could quench, if the magnet temperature increases above a certain value, the pressure could only be increased by approximately one order of magnitude. Still, no discharges have been observed. However, a correlation between the pressure and the leakage current at the detector electrode is evident as can be seen from Fig. 3.29). The influence of the pressure on the leakage current seems to decrease rapidly below a pressure of about 5×10^{-9} mbar, cf. Fig. 3.30.

During the 2012 background measurements, similar discharge tests have been performed, in which the vacuum has been worsened by the

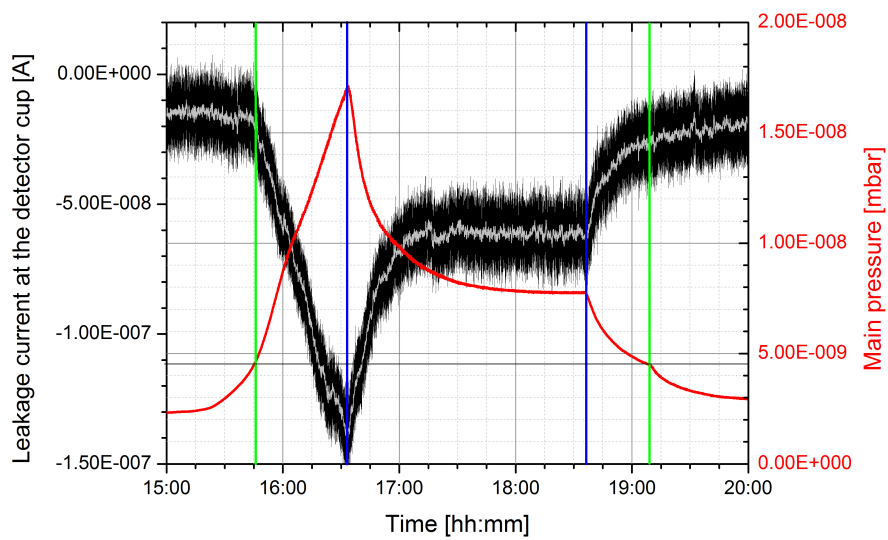


Figure 3.30: Zoom of Fig.3.29: During the bake-out of the spectrometer *a*SPECT the pressure starts to increase, while the leakage current at the detector cup does not change until the first green line is reached. Then the leakage current instantly alternates with the pressure. The fast reaction can be clearly seen at the blue lines. Beyond the second green line the dependency seems to decrease again, at a pressure of about 5×10^{-9} mbar.

introduction of Helium into the spectrometer through a needle valve. In principle, the advantage of this method is, that higher pressures can be achieved and that the pressure valve can be set more precisely. The latter could not be achieved in summer 2012, because of a not fine enough needle valve. Furthermore, the internal getter pumps can be over-saturated. Penning traps eliminated by these getter pumps could be present again and the chance for discharges might increase. Our rudimentary tests with Helium also could not provoke discharges. These and all other background measurements with the detector installed have been subject to detailed analysis and are presented in [24].

In summary, our off-line background measurements showed that the *a*SPECT spectrometer has been improved sufficiently and is now ready for a new measurement of the electron-antineutrino correlation coefficient *a*. In addition, the background measurements revealed a clear correlation between gas pressure and leakage current. Based on the positive experience with the off-line background measurements, I propose to repeat those tests with the re-designed detector electrode (for details see Sect. 3.2).

3.5 Latest status of the background measurements

As mentioned above, the *a*SPECT spectrometer has been improved sufficiently for the latest beam time in summer 2013 at ILL. Figure 3.31 shows the temporal evolution of the background count rate during a measurement of this beam time. Compared to Figs. 3.3 and 3.4, the background count rate dropped below the level of the 2008 beam time. This confirms the results of the off-line measurements presented in the last section (see also Ref. [24]).

Furthermore, the installation of an additional $\vec{E} \times \vec{B}$ electrode inside the AP, instead of the AP electrode e15 (cf. Fig. 3.6), nearly eliminated the AP voltage dependence of the background count rate [26]. More details are to be found in the Ph.D. thesis of R. Maisonobe [24].

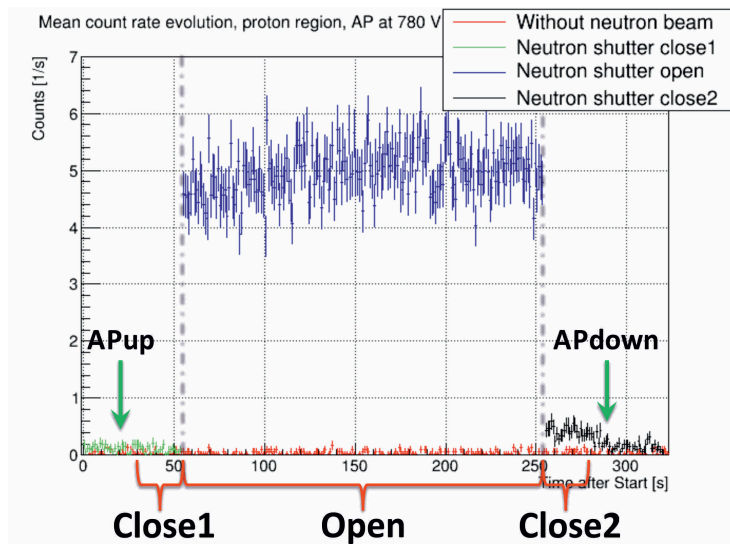


Figure 3.31: The temporal evolution of the background count rate measured at $U_A = 780$ V, typical example of the latest beam time in summer 2013 at ILL; taken from [26]. To illustrate, the dashed gray lines show when the neutron shutter was opened and later closed again. The comparison with Figs. 3.3 and 3.4 shows that the background count rate dropped below the 2008 level.

Chapter 4

Evaluation of the magnetic field measurements in 2011

In Sect. 2.5.2, the influence of the uncertainty in the magnetic field ratio $r_B = B_A/B_0$ Eq.(2.11) on the relative error in the electron-antineutrino correlation coefficient a has been discussed. For the goal accuracy of 0.3 %, the magnetic field ratio r_B has to be known with a relative accuracy of 1×10^{-4} . To this end, the magnetic field of the a SPECT magnet has been measured as part of F. Ayala Guardia's Ph.D. thesis [5] in winter 2007/08 with a Hall-effect sensor (and later a proton (^3He) NMR magnetometer). Due to a lack of Hall probe calibration, the relative uncertainty in the magnetic field ratio exceeded 1×10^{-3} , too much for a 1 % measurement of a . Hence, the magnetic field measurement has been repeated in spring 2011. The data of this measurements have not until now been analyzed as there have been considerable doubts about the quality of this measurement, due to the instability of the hall probe in used. For the latest beam time in summer 2013, the a SPECT Collaboration had to decide whether or not another magnetic field measurement is necessary. Therefore, the data of 2011 are analyzed now, as a part of this Master thesis. In this chapter, a short description of the systematics of the Hall probe are given. Furthermore the corrections which must be applied to the measurement data are explained. Finally, the 2011 measurement will be compared with earlier measurements and the relative error in a due to the uncertainty in r_B will be estimated. All magnetic field measurements presented in this chapter were taken in the 'standard' configura-

Table 4.1: Specifications of the MPT-141 Hall probe [1]: The systematic errors and corrections have been calculated for the 3.0 T range in the decay volume (DV) and both for the 0.6 T and 3.0 T range in the analyzing plane (AP). Input values: 0.44 T (AP) and 2.18 T (DV). For the probe cable, the actual length of 10 m was inserted.

	DV [Gauss]	AP, 3 T R. [Gauss]	AP, 0.6 T R. [Gauss]
Absolute Accuracy:			
± 0.006 % of full scale at 25°C	± 1.8	± 1.8	± 0.36
± 0.01 % of reading at 25°C	± 2.18	± 0.44	± 0.44
Temperature stability:			
scale factor:			
± 10 ppm of reading/°C, max	$\pm 0.22/^\circ\text{C}$	$\pm 0.04/^\circ\text{C}$	$\pm 0.04/^\circ\text{C}$
± 5 ppm of reading/°C, typical	$\pm 0.11/^\circ\text{C}$	$\pm 0.02/^\circ\text{C}$	$\pm 0.02/^\circ\text{C}$
zero drift (max):	$\pm 0.1/^\circ\text{C}$	$\pm 0.1/^\circ\text{C}$	$\pm 0.03/^\circ\text{C}$
$\pm(1 \mu\text{T}+0.0003$ % of full scale)/°C			
effect of probe cable: -3 ppm/°C of reading/meter of probe cable	$-0.65/^\circ\text{C}$	$-0.65/^\circ\text{C}$	$-0.13/^\circ\text{C}$

tion $I_{\text{main}} = 70$ A, $I_3 = 35$ A, $I_5 = 15$ A, $I_{12} = -I_{13} = 25.5$ A and $I_{14} = I_{15} = 0$ (for details see [4]).

4.1 Accuracy and stability of the MPT-141 Hall probe

In this section, the influence of the Hall probe accuracy on the magnetic field measurement will be discussed. Table 4.1 summarizes the associated information from the data sheet of the Hall probe used; a Group 3 Technologies miniature Hall probe, MPT-141 [1] (for the data sheet see App. B). The probe can measure in four different ranges: 0.3T(range 0), 0.6T(range 1), 1.2T(range 2) and 3.0T(range 3). Since the magnetic field of *a*SPECT varies between 0.44T in the AP, 2.18T in the DV and 4.4T at the proton detector, the 3.0 Tesla and the 0.6 Tesla range have been used for the measurements.

First, we neglect the temperature effects(see later in Sect. 4.2). For reasons of measurement stability, it was discussed to only use the 3.0 Tesla range, both for the analyzing plane(AP) and for the decay volume(DV). In the DV only the 3.0T range can be used as in other ranges the probe would be out of range. By using Equ.(2.24), the

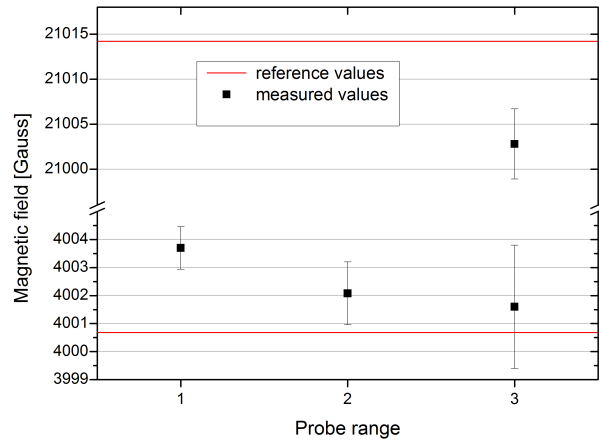


Figure 4.1: Test calibration measurements of the MPT-141 Hall probe performed by Group 3 in October 2011 (see. App. B); upper limits of the magnetic field: range 1: 0.6 T, range 2: 1.2 T, range 3: 3.0 T. The drift since the calibration in 2006 is similar to the drift between 2002 and 2006 (for details see Ref. [5] and the text): In range 1, the deviation in the AP region is approximately 3 Gauss, in Range 3 in the DV it is approximately 11.5 Gauss.

absolute accuracy of the Hall probe yields an uncertainty in r_B of:

$$\Delta r_B^{absolute\ uncertainty} = \begin{cases} \pm 1.10 \times 10^{-4} & , \text{ AP in 3.0T range} \\ \pm 0.52 \times 10^{-4} & , \text{ AP in 0.6T range} \end{cases} \quad (4.1)$$

The Hall probe exhibits long-term drift and therefore has been calibrated in 2002 and in 2006. In this time period, the 3.0T range of the probe drifted by about 10 Gauss in the DV and 4 Gauss in the AP, respectively. In a lack of probe calibration in 2008, these values have been used for the error estimation of the 2008 data [5]. Consequently, a further calibration for the analysis of the 2011 measurements was absolutely necessary. In 2006, the last corrections have been implemented in the read-out electronics of the probe. In 2011, test(the 'standard' calibration of the probe was impossible, due to the broken temperature sensor of the probe) measurements have been performed by the probe manufacturer four months after the magnetic field measurements inside *a*SPECT. In the data analysis, these serve as an estimation for the error by the lacking calibration. Figure 4.1 shows the deviation between the reference values and the indicated values (read-out 'corrected' by 2006 calibration). For the first calibration in 2002, 15 different magnetic field values have been measured. The manufacturer then provided a scaling factor and the zero off-set, which allow the calculation of the corrections for any value of the magnetic field. As mentioned above, in 2011, a 'standard' calibration was impossible. Hence, the test field points

21014.2 Gauss and 4000.68 Gauss

close to the magnetic field in the DV (21700 Gauss) and in the AP (4415 Gauss) have been chosen. Missing a number of calibration field points to extract scaling factor and zero off-set, we first must investigate the fact that the test field points are not exactly our measurement points. Therefore, we compare the absolute correction of the associated values in 2006 with respect to the 2002 calibration. The result is summarized in Table 4.2. Obviously, the influence is rather small.

Table 4.2: Influence of the fact that the test field points of 2011 are not exactly our measurement points.

B [Gauss]	ΔB^{2006} calibration [Gauss], 3 T range	ΔB^{2006} calibration [Gauss], 0.6 T range
4000.68	+3.53	-2.26
4015	+3.69	-2.54
ΔB^{2011} field point	± 0.16	± 0.28
21014.2	10.17	-
21700	10.13	-
ΔB^{2011} field point	± 0.06	-

Since there were four months between the 2011 magnetic field measurements and the 2011 probe calibration, we must consider the drift of the probe in this time period. For this, we take the drift between 2006 and 2011 and scale it down to four months. This results in additional uncertainties:

$$\Delta B^{2011 \text{ calibration}} = \begin{cases} \pm 0.20 \text{ Gauss} & , \text{ AP in 0.6 T range} \\ \pm 0.06 \text{ Gauss} & , \text{ AP in 3 T range} \\ \pm 0.77 \text{ Gauss} & , \text{ DV} \end{cases} \quad (4.2)$$

By summing up the probe inaccuracies Table 4.1 (neglecting temperature effects) and the calibration influences Table 4.2 and Eq. (4.2) we obtain

$$\Delta B^{\text{accuracy \& stability}} = \begin{cases} \pm 1.28 \text{ Gauss} & , \text{ AP in 0.6 T range} \\ \pm 2.46 \text{ Gauss} & , \text{ AP in 3 T range} \\ \pm 4.81 \text{ Gauss} & , \text{ DV} \end{cases} \quad (4.3)$$

and consequently

$$\Delta r_B^{\text{accuracy \& stability}} = \begin{cases} \pm 0.74 \times 10^{-4} & , \text{ AP in 0.6 T range} \\ \pm 1.22 \times 10^{-4} & , \text{ AP in 3 T range} \end{cases} \quad (4.4)$$

by substituting Eq. (4.4) into Eq. (2.24).

4.2 Temperature effects and zero offset

The read-out device (DTM-151) of the Hall probe compensates the temperature drift of the probe. The temperature scale factor and the zero drift given in Table. 4.1 have to be added to the systematic error bar, as they are uncertainties of the temperature compensation. For the temperature scale factor, we assume the maximum and not the typical value, because we like to get a worst case estimation. During the magnetic field measurements in 2011, for the determination of the magnetic field ratio r_B , a maximum temperature difference of about 2°C from the calibration value of 25°C occurred. Combining the accuracy, stability, temperature effects and zero offset, this yields:

$$\Delta B^{\text{sys.}} = \begin{cases} \pm 1.42 \text{ Gauss} & , \text{ AP in 0.6 T range} \\ \pm 2.74 \text{ Gauss} & , \text{ AP in 3 T range} \\ \pm 5.45 \text{ Gauss} & , \text{ DV} \end{cases} \quad (4.5)$$

and consequently

$$\Delta r_B^{\text{sys.}} = \begin{cases} \pm 0.83 \times 10^{-4} & , \text{ AP in 0.6 T range} \\ \pm 1.36 \times 10^{-4} & , \text{ AP in 3 T range} \end{cases} \quad (4.6)$$

Additionally, the length of the cable from the Hall probe to the read-out device has to be taken into account. This correction is directly applied to the measurement data and does not influence the error estimation. In addition, the zero offset O_{zero} of the probe was measured inside a μ -metal box at the beginning of every measurement sequence. It has to be subtracted from the measurement data. Taking into account the zero offset and the temperature correction C_{cable} due to the cable length, one obtains:

$$B = B_{\text{readout}} - O_{\text{zero}} - C_{\text{cable}} \quad (4.7)$$

As mentioned above, during the calibration of the Hall probe in October 2011, it turned out that the temperature compensation was open circuit. Therefore we need to know, whether this malfunction

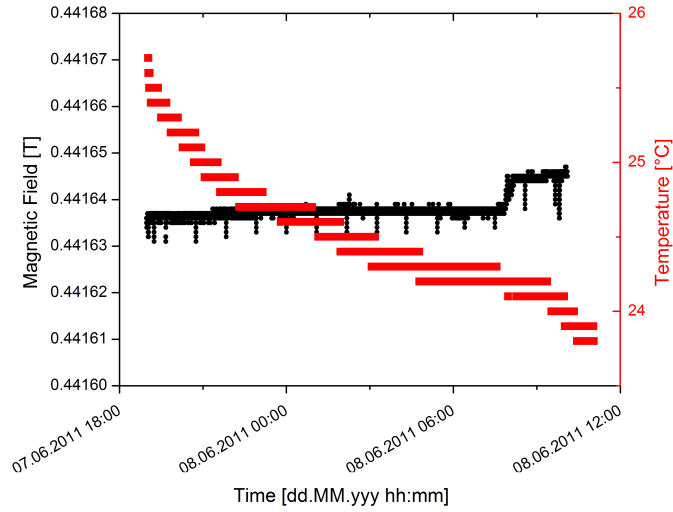


Figure 4.2: Continuous magnetic field measurement in 2011 with the Hall probe MPT-141 in the 0.6 T range; measurement time approximately 15.5 hours. The measured field drifts only by 0.2 Gauss, while the temperature decreases by 2°C.

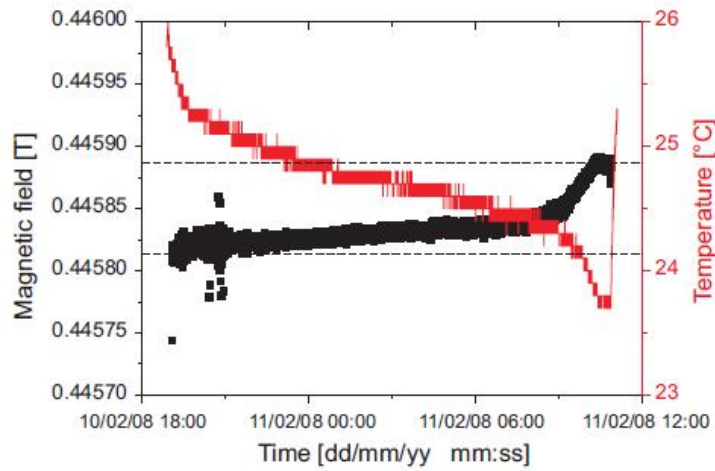


Figure 4.3: Continuous magnetic field measurement in 2008 with the Hall probe MPT-141 in the 0.6 T range, taken from [5]: The measured field drifts by approximately 0.7 Gauss, while the temperature decreases by 2°C.

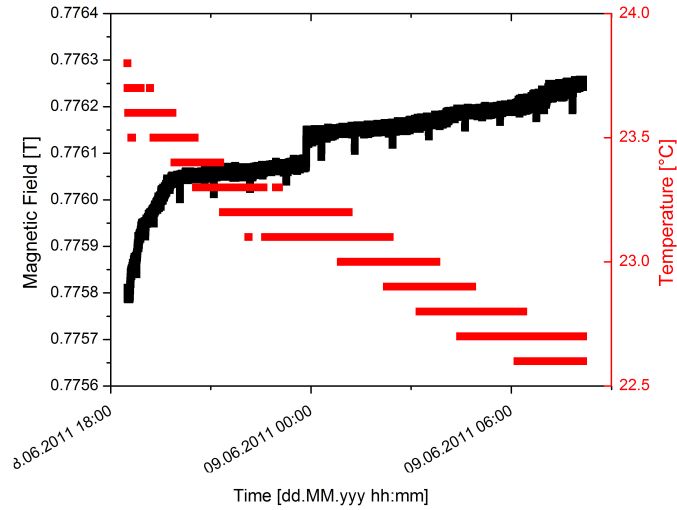


Figure 4.4: Continuous magnetic field measurement in 2011 with the Hall probe MPT-141 in the 3.0 T range: The measured field drifts by approximately 5 Gauss, while the temperature decreases by 2.5°C.

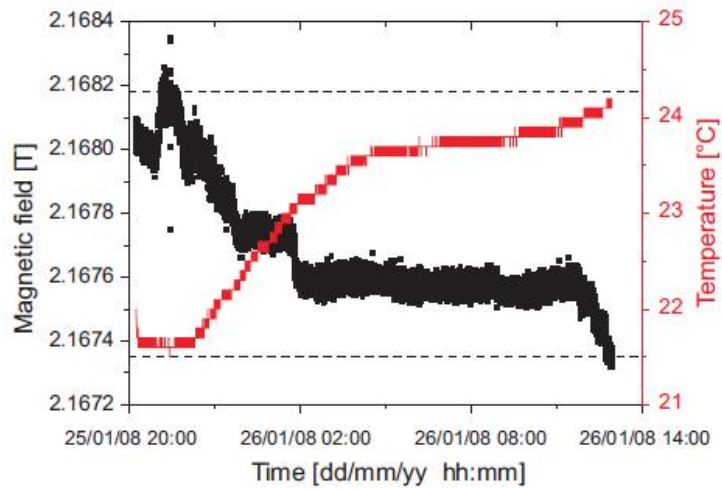


Figure 4.5: Continuous magnetic field measurement in 2008 with the Hall probe MPT-141 in the 3.0 T range, taken from [5]: The measured field drifts by approximately 8 Gauss, while the temperature increases by 2.5°C.

was already present during the 2008 and/or 2011 measurements. In 2011, two long-term measurements have been performed, one in the 0.6 Tesla and one in the 3.0 Tesla range shown in Fig. 4.2 and Fig. 4.4, respectively. Comparing these continuous measurements with similar ones in 2008, shown in Fig. 4.3 and Fig. 4.5, respectively, one can see that the drifts are quite comparable. However, the drifts of the order of 2.5 Gauss/° C or more cannot be explained by the uncertainties in the temperature correction for the probe and the probe cable (cf. Table 4.1). Hence, it is obvious that the temperature correction did not work properly, the mounting of the probe is not sufficiently stable or the functionality of the teslameter is not well understood. In the first case we can estimate the additional errors to

$$\Delta B^{\text{temp.}} = \begin{cases} 0.2 \text{ Gauss} & , \text{ AP in 0.6 T range} \\ 4.0 \text{ Gauss} & , \text{ DV and AP in 3 T range} \end{cases} \quad (4.8)$$

and

$$\Delta r_{\text{B}}^{\text{temp.}} = \begin{cases} \pm 0.39 \times 10^{-4} & , \text{ AP in 0.6 T range} \\ \pm 1.88 \times 10^{-4} & , \text{ DV and AP in 3 T range} \end{cases} \quad (4.9)$$

This is too high for an 1 % measurement of a . Hence, it is of uttermost importance, to test the long-term stability of the Hall probe, temperature stabilized and in the dependence of the ambient, probe and cable temperature. The second case can be almost entirely excluded, as the unintended lowering of the probe in the AP would correspond to a decrease of the magnetic field, while in the DV to an increase, both in contrast to Figs. 4.2 and 4.5.

4.3 Decrease of the magnetic field

The main magnetic field is generated by superconducting coils which show the highest stability in persistent mode¹. In this mode, the current in the coils and therefore the magnetic field decreases slowly with time after the ramping-up procedure [5]. The effect has been

¹In persistent mode, the superconducting coils are short-circuited and separated from the power supply after ramping, whereas in normal mode the coils are constantly energized.

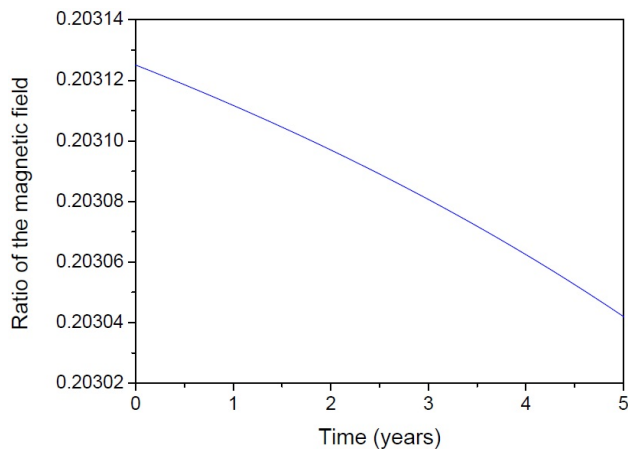


Figure 4.6: Temporal decrease of the magnetic field ratio r_B caused by the decrease of the magnetic field in persistent mode, taken from [5].

measured with a Nuclear Magnetic Resonance (NMR) magnetometer and can be expressed as [5]:

$$B(t) = B - \frac{\Delta B}{\Delta t}t \quad (4.10)$$

with

$$\frac{\Delta B}{\Delta t} = \begin{cases} (-0.571 \pm 0.014) \text{ Gauss/d} & , \text{ AP} \\ (-2.81 \pm 0.07) \text{ Gauss/d} & , \text{ DV} \end{cases} \quad (4.11)$$

where t is the time between switching-off the main heater, after ramping up the coils, and the measurement itself.

We note that the normal conducting correction coils are not operated in persistent mode. Therefore their current and magnetic field are constant. However, the influence on Eq. 4.11 has been calculated and is negligible [5]. For absolute field measurements the corrections Eqs. (4.10) and (4.11) must be applied to the data. For the calculation of r_B the measurement data are usually recorded within half an hour. Furthermore the correction for the DV and AP have the same direction. In summary, the influence on the magnetic field ratio has been calculated in Ref. [5] and is very small, as we can see in Fig.4.6. Therefore the decrease of the magnetic field with time has been neglected for the calculation of r_B .

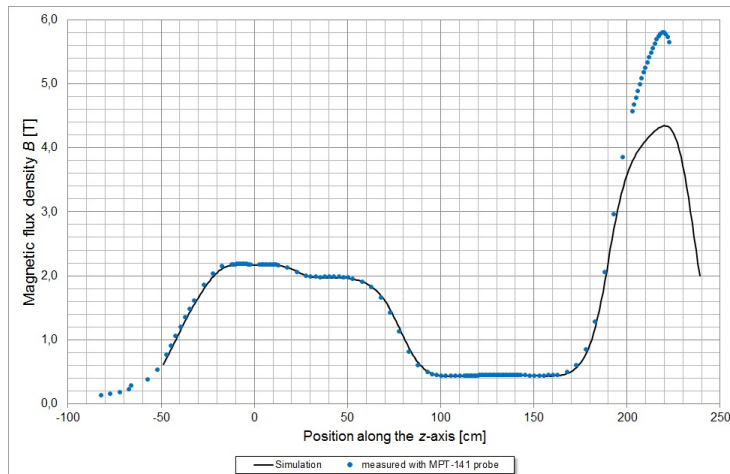


Figure 4.7: The magnetic field profile along the z -axis of the a SPECT spectrometer. The blue points show a measurement with the Group3 Hall probe in comparison with a simulation (black). See the text for details. The profile was measured at $I_{\text{main}} = 70$ A, $I_3 = 35$ A, $I_5 = 15$ A, $I_{12} = -I_{13} = 25.5$ A and $I_{14} = I_{15} = 0$.

4.4 Shape of the magnetic field

Obviously, the Hall probe (Group3 MPT-141) used for the mapping of the a SPECT magnetic field is limited to a maximum magnetic field of 3.0 Tesla. Hence, 'precision' measurements of the magnetic field at height of the proton detector ($z \approx 2.2$ m) have failed up to now [4, 5], as can also be seen from Fig. 4.7.

For the magnetic field measurements in 2011, the field has therefore also been mapped with an high-linearity Hall probe Arepoc HHP-SF 662 (for details see B.7 and [2]). At $T = 300$ K and $B = 0 - 1$ T, the linearity error of this probe is $< 0.5\%$. The Arepoc HHP-SF probe is suitable for operation at a temperature range of 1.5 – 350 K in magnetic fields up to 5 Tesla. Figure 4.8 shows the magnetic field measured with this probe in comparison with a simulation of the a SPECT field. In the AP, no obvious deviation from the simulation is visible, contrary to the DV and the high-field region around the proton detector.

However, the Arepoc probe differs by only a few % from the simulations, whereas the Group3 probe differs by up to 34%, as can be seen from the comparison of Figs. 4.7 and 4.8 as well from the

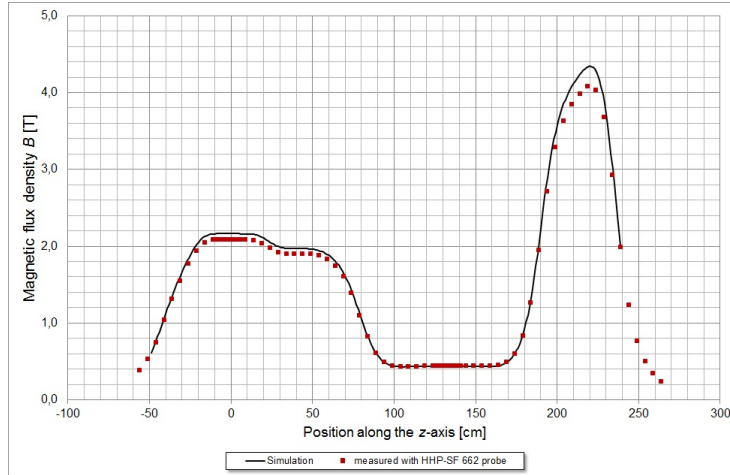


Figure 4.8: The magnetic field profile along the z -axis of the a SPECT spectrometer. The red points show a measurement with the Arepoc Hall probe in comparison with a simulation (black). See the text for details. The profile was measured at $I_{\text{main}} = 70$ A, $I_3 = 35$ A, $I_5 = 15$ A, $I_{12} = -I_{13} = 25.5$ A and $I_{14} = I_{15} = 0$.

residuals shown in Fig. 4.9. In this way, the simulated maximum of the a SPECT magnetic field (at height of the proton detector) could be confirmed to about 6%, which is sufficient for, e.g., calculations of the edge effect (for details see Ref. [23]).

In the AP, the experimental data points perfectly match the simulated field values, to $< 0.3\%$ in accordance with the probe specifications (see App. B). In contrast, in the DV, the experimental data points exceed/fall below the simulated field values by $> 0.5\%$. For the Group3 probe, the deviation of 'only' 0.7% has already been observed in earlier magnetic field studies. But, it can be attributed to the moderate knowledge of the magnetization curves of the a SPECT field return yoke (for details see Ref. [23]). For the Arepoc probe, the deviation of 3.7% can be attributed to a lack of probe calibration, more precisely a scaling factor for magnetic fields above 1 Tesla. In addition, the position of the maximum of the magnetic field has been confirmed to $z = 2.20(1)$ m.

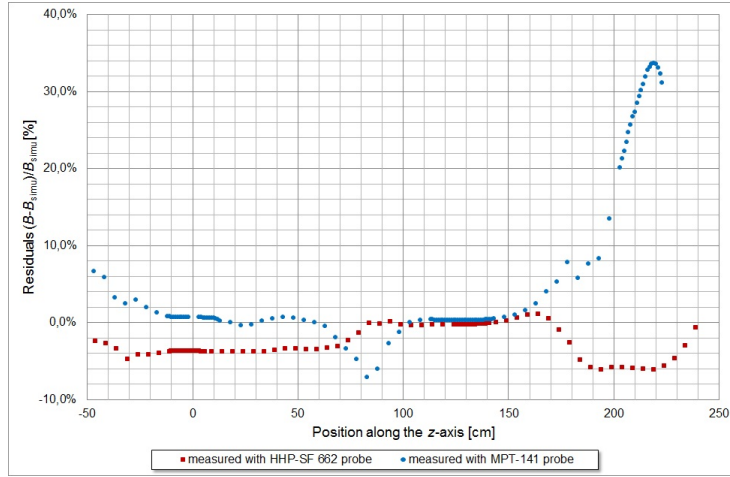


Figure 4.9: The residuals of the measured magnetic field profiles, presented in Figs. 4.7 and 4.8, from a simulation of the *a*SPECT magnetic field. Obviously, the Arepoc probe differs by only a few % from the simulations, whereas the Group3 probe differs by up to 34%. See the text for details. The profiles were measured at $I_{\text{main}} = 70$ A, $I_3 = 35$ A, $I_5 = 15$ A, $I_{12} = -I_{13} = 25.5$ A and $I_{14} = I_{15} = 0$.

4.5 Determination of the magnetic field ratio r_B

The importance of the precision knowledge of the magnetic field ratio r_B for a precise measurement of a with the spectrometer *a*SPECT has been discussed in Sect.2.5.2. Based on the experience gained during the magnetic field measurements in 2005 [4], 2006 and 2008 [5], the following measurement procedure has been proposed [5]:

1. Select the appropriate scale for the region to measure (3 T range for the DV and 0.6 T range for the AP).
2. Zero the Hall probe inside a zero-field region (here μ -metal box).
3. Measure the remaining zero offset after zeroing the probe inside the μ -metal box.
4. Measure the magnetic field at the regions of interest in steps of 1 cm along the (z -)symmetry axis, recording the field, the temperature and time.

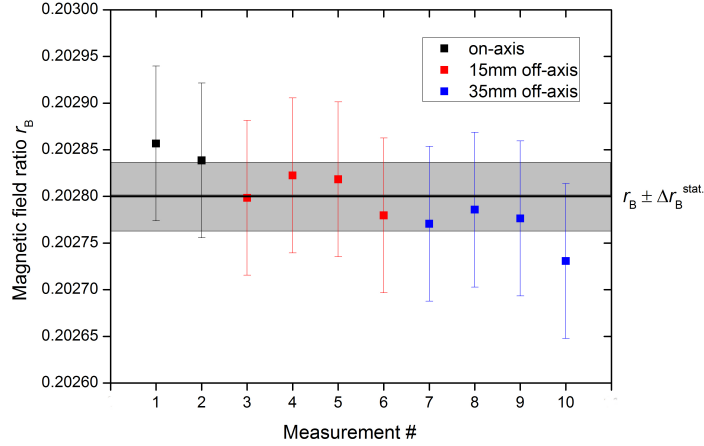


Figure 4.10: Calculated values for r_B from the 2011 magnetic field measurements in the 3.0 T range (DV) and in the 0.6 T range (AP), on- and off-axis. Error bars show systematic errors only. For elucidation of the much better reproducibility, the mean value with its statistical error bar is also shown (black line and gray bars).

5. Measure the drift of the probe (zero offset) inside the μ -metal box².
6. Apply all corrections.

For measurements taken according to this procedure, the systematic error in r_B is then given by Eq. (4.6). Taking into account the 2011 test measurements, the following corrections are applied in the DV (cf. Sect. 4.1):

$$B_{\text{corrected}}[\text{Gauss}] = B_{\text{meas}}[\text{Gauss}] + 11.4 \text{ Gauss} \quad (4.12)$$

and in the AP

²This value has not been used to correct the measurement data but serves to exclude 'bad' data.

Table 4.3: Mean value and statistical error of r_B calculated for the values shown in Fig. 4.10, systematical error according to Eq.(4.6) and the influence of both errors on the correlation coefficient a (for details see Sect. 2.5.2).

r_B	statistical error(σ)	systematic error	$\Delta a/a[\%]$
0.20280	0.37×10^{-4}	0.83×10^{-4}	0.44

$$B_{\text{corr}}[\text{Gauss}] = B_{\text{meas}}[\text{Gauss}] - \begin{cases} 3.02 \text{ Gauss} & , \text{ AP in 0.6 T range} \\ 0.92 \text{ Gauss} & , \text{ AP in 3.0 T range} \end{cases} \quad (4.13)$$

Furthermore the offset and temperature correction Eq.(4.7) has been applied to the data.

The magnetic field has been measured on-axis as well as off-axis at radial distances of 15 mm and 35 mm. The results are plotted in Fig. 4.10. Obviously, the values of r_B vary for less than the systematic error bars. In Table 4.3 the mean value, the statistical and the systematic error of r_B as well as the influence on a are presented.

In order to measure in two scales/ranges, the probe has to be removed from the magnet and zeroed in the μ -metal box. This increases the time between the measurements in the AP and in the DV unnecessarily. The probe's time and temperature drift will therefore increase. On the other hand, an additional uncertainty in the mounting of the probe will occur. For those reasons it was decided to change, respectively improve, the data recording as follows [3]:

- use only one scale/range of the Hall probe (necessarily the 3 T range)
- evaluate r_B only from measurements performed in a short time period

The results of the magnetic field measurements only in range 3 are plotted in Fig. 4.11 and summarized in Table 4.4. The much smaller statistical error can be understood as a confirmation of the improved

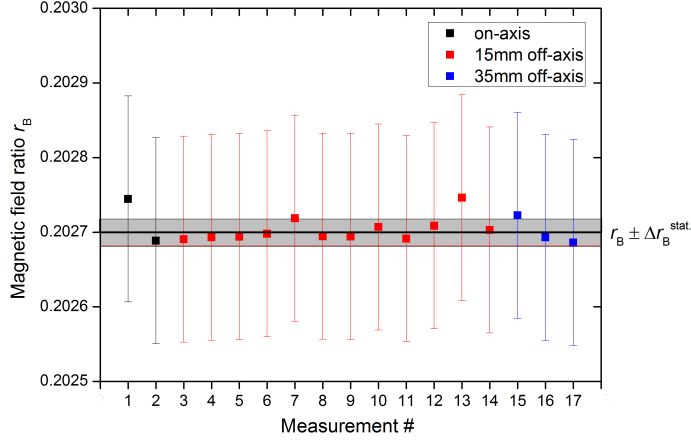


Figure 4.11: Calculated values for r_B from the 2011 magnetic field measurements in the 3.0 T range, on- and off-axis. Error bars show systematic errors only. For elucidation of the much better reproducibility, the mean value with its statistical error bar is also shown (black line and gray bars).

Table 4.4: Mean value and statistical error of r_B calculated for the values shown in Fig. 4.11, systematic error according to Eq. (4.6) and the influence of both errors on the correlation coefficient a (for details see Sect. 2.5.2).

r_B	statistical error(σ)	systematic error	$\Delta a/a[\%]$
0.20270	1.85×10^{-5}	1.36×10^{-4}	0.67

way of data taking (and not only attributed to double the number of measurements). But, neglecting the additional uncertainty in r_B by the positioning/mounting of the probe, measurements in one range only are inferior to measurements in two ranges by nearly double the systematic error, cf. Table 4.3.

Finally, the results presented above are compared with each other and with the results of the 2008 measurements. All on- and off-axis measurements are shown in Fig. 4.12. The 2008 measurements have been performed in two ranges of the Hall probe (in the 0.6 and in the 3.0 T range). The closest calibration of the probe has been carried out in 2006. In the data analysis prior to the 2011 test calibration measurements, therefore a calibration error of

$$\Delta B^{2008 \text{ 'calibration'}} = \begin{cases} \pm 4 \text{ Gauss} & , \text{ AP in 0.6 T range} \\ \pm 10 \text{ Gauss} & , \text{ DV} \end{cases} \quad (4.14)$$

has been assumed [5]. For this estimation, the drift between 2002 and 2006 served as a reference. Adding the systematic error calculated from Table 4.1 the total systematic error is approximately

$$\Delta B^{2008, \text{ syst.}} = \begin{cases} \pm 5 \text{ Gauss} & , \text{ AP in 0.6 T range} \\ \pm 14 \text{ Gauss} & , \text{ DV} \end{cases} \quad (4.15)$$

The resulting systematic error in r_B has been used for the error bars of the 2008 data shown in Fig. 4.12. As can be seen, these error bars overlap with those of all 2011 measurements, but not with the mean value of the range 3 only measurements. This might indicate that

- the systematic error due to a missing calibration in 2008 is still underestimated
- the systematic uncertainty due to the non-'standard' calibration in 2011 is underestimated
- the influence of a potential malfunction of the temperature correction is underestimated and/or cannot be neglected
- the systematic uncertainty due to the re-positioning of the probe for measurements in two ranges cannot be neglected, neither in 2008 nor in 2011

In this thesis, the 2008 data are therefore not used for the calculation of r_B .

Although it has been decided not to use the measurements in different ranges [3], the mean value and the statistical error for all 2011 measurements have been calculated in order to get an idea of the error magnitude, and are presented in Table 4.5.

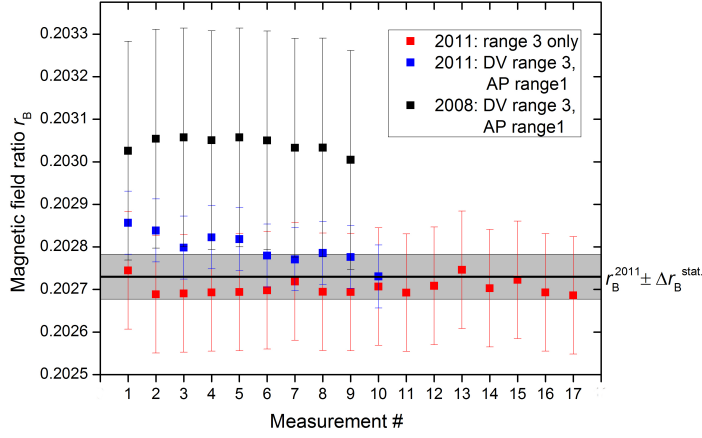


Figure 4.12: Calculated values for r_B from 2008 and 2011. Obviously, the 2008 values are much higher, which is most likely caused by the missing calibration. Error bars show systematic errors only. For elucidation of the much better reproducibility, the mean value with its statistical error bar is also shown (black line and gray bars).

Table 4.5: Mean value and the statistical error of r_B for the values shown in Fig. 4.10 and Fig. 4.11, as well as the influence on the correlation coefficient a .

r_B	statistical error(σ)	$\Delta a/a[\%]$
0.20273	0.53×10^{-4}	0.26

4.6 Conclusion

The magnetic field measurements in 2008 and in 2011 yield deviating results such that they cannot be used both to announce a value for the magnetic field ratio r_B (for details see Sect. 4.5). The 2008 value is most likely much worse due to a lack of probe calibration within a reasonable time frame. Nevertheless, the test measurements of the probe in October 2011 do not exhibit the same quality as the calibrations before. As expected the statistical error for measurements in different probe ranges is much higher than for measurements in the same range. This confirms the decision to only use data from single range measurements. However, the systematic error then increases and might limit the total error unnecessarily. In Ref. [5] it has been suspected that for the measurement of a ratio of magnetic fields in the same probe range it could be enough to consider the statistical error only. In my opinion, a detailed characterization of the Hall probe is mandatory to confirm this hypotheses. The total error of r_B presented in Table 4.4, results in a relative error in the correlation coefficient a of

$$\frac{\Delta a}{a} = 0.67\% \quad (4.16)$$

This is difficult to be accepted, even for an 1 % measurement of a . Hence, another measurement of the magnetic field including a new calibration of the Hall-probe after the beam time in 2013 was mandatory. The new calibration confirms the large long-term drift of the probe (about 18 Gauss in the DV, cf. App. B). The systematic error for the 2011 magnetic field measurements could still be underestimated due to the broken temperature correction (cf. Sect. 4.2). For the 2013 magnetic field measurements, the temperature correction has been repaired and the probe has been calibrated. Therefore, the systematic error will decrease, which will be sufficient for an 1 % measurement of the correlation coefficient a . In order to get closer to the design goal of the a SPECT spectrometer, which is to determine a with a relative error of 0.3 %, a detailed characterization of the Hall probe is mandatory. As mentioned before, the probe accuracy still limits the relative error in a to 0.26 %.

Chapter 5

Summary and Outlook

The spectrometer *a*SPECT has been built to measure the electron-antineutrino correlation coefficient a with a relative accuracy of 0.3%. For the determination of a from the proton recoil spectrum, the analyzing plane voltage U_A and the magnetic field ratio r_B need to be known with high precision. The influence of uncertainties in these quantities on the relative error in a has been calculated in detail. For the magnetic field ratio r_B , a linear dependence between the relative uncertainties in a and r_B has been derived. This has been used to estimate the quality of the magnetic field measurements in 2011.

Severe background problems during earlier beam times prevented the *a*SPECT Collaboration from presenting a new value for a so far. After the 2011 beam time, further improvements of the spectrometer were inevitable. Several improvements of the electrode system and of the vacuum system yielded reasonable results during off-line background measurements in 2012. For future beam times, the (high-voltage) detector electrode has been re-designed as part of this thesis. In the new design, the high electric field at the surface of this electrode, responsible for field emission of electrons, has been significantly reduced. The new detector electrode has been finished in summer 2013 and can be used for upcoming measurements.

Currently, the data of the 2013 beam time is being analyzed. To this end, the magnetic field ratio r_B needs to be determined. The magnetic field of the *a*SPECT magnet has been mapped with a

Hall effect sensor, in 2005/06, 2008 and 2011. As part of this thesis, the 2011 measurements have been evaluated and compared with the former measurements and their results. The analysis revealed that a lack of 'standard' probe calibration presently limits the relative accuracy in r_B to $\Delta r_B/r_B = 6.76 \times 10^{-4}$, what corresponds to $\Delta a/a = 0.67\%$. This made it necessary to repeat the magnetic field measurements including probe calibration after the beam time in summer 2013.

The analysis of the probe specifications showed that the measurement of the magnetic field with the Hall probe limits the achievable accuracy in r_B to $\Delta r_B/r_B = 2.56 \times 10^{-4}$, what corresponds to $\Delta a/a = 0.26\%$. For an 1%-measurement of a , this is sufficient. To reach the goal accuracy in a of 0.3%, an on-line proton NMR magnetometer has been developed [5], with $\leq 2 \times 10^{-5}$ relative precision, which currently is being improved and has been tested during and after the 2013 beam time.

In addition, the comparison with the 2008 magnetic field measurements confirmed that large systematic errors have to be assigned to the 2008 data, because of the missing probe calibration.

Appendices

Appendix A

Detailed calculations on the measuring accuracy

At first, we will calculate the derivative of the numerator of Eq. (2.12) with respect to U_A :

$$\begin{aligned} \frac{d(\text{Numerator})}{dU_A} = & \frac{d}{dU_A} \underbrace{\left(\int_{T_{\text{tr}}^{\min}}^{T_{\text{tr}}^{\max}} \left(1 - \sqrt{1 - \frac{B_0}{B_A} \left(1 - \frac{eU_A}{T} \right)} \right) g_1(T) dT \right)}_{\text{I}} \\ & + \underbrace{\int_{T_{\text{tr}}^{\max}}^{T_{\text{p,max}}} g_1(T) dT}_{\text{II}} - r_h(U_A) \underbrace{\int_0^{T_{\text{p,max}}} g_1(T)}_{\text{III}} \end{aligned} \quad (\text{A.1})$$

Both integration limits of the first integral and the lower integration limit of the second integral depend on U_A . Therefore, we have to use Eq. (2.14).

$$\begin{aligned}
\frac{d(\mathbf{I})}{dU_A} &= \frac{d}{dU_A} \int_{T_{\text{tr}}^{\min}}^{T_{\text{tr}}^{\max}} \left(1 - \sqrt{1 - \frac{B_0}{B_A} \left(1 - \frac{eU_A}{T}\right)}\right) g_1(T) dT = \\
&= \int_{T_{\text{tr}}^{\min}}^{T_{\text{tr}}^{\max}} \frac{\partial}{\partial U_A} \left(1 - \sqrt{1 - \frac{B_0}{B_A} \left(1 - \frac{eU_A}{T}\right)}\right) g_1(T) dT \\
&+ \frac{d}{dU_A} (T_{\text{tr}}^{\max}) (F_{\text{tr}}(T_{\text{tr}}^{\max}; U_A) g_1(T_{\text{tr}}^{\max})) \\
&- \frac{d}{dU_A} (T_{\text{tr}}^{\min}) (F_{\text{tr}}(T_{\text{tr}}^{\min}; U_A) g_1(T_{\text{tr}}^{\min})) \tag{A.2}
\end{aligned}$$

with the transmission function at the integration limits

$$F_{\text{tr}}(T_{\text{tr}}^{\min}; U_A) = 0$$

$$F_{\text{tr}}(T_{\text{tr}}^{\max}; U_A) = 1 \tag{A.3}$$

and the derivatives of the integration limits

$$\frac{d}{dU_A} (T_{\text{tr}}^{\max}) = \frac{e}{1 - \frac{B_A}{B_0}}$$

$$\frac{d}{dU_A} (T_{\text{tr}}^{\min}) = e \tag{A.4}$$

this yields:

$$\frac{d(\mathbf{I})}{dU_A} = - \int_{T_{\text{tr}}^{\min}}^{T_{\text{tr}}^{\max}} \frac{e}{2r_B T \sqrt{1 - \frac{B_0}{B_A} \left(1 - \frac{eU_A}{T}\right)}} g_1 dT + \frac{e}{1 - \frac{B_A}{B_0}} g_1(T_{\text{tr}}^{\max}) \tag{A.5}$$

The integrand of the second integral does not depend on U_A , but the lower integration limit does. Therefore, we get only one term

$$\frac{d(\mathbf{II})}{dU_A} = \frac{d}{dU_A} \int_{T_{\text{tr}}^{\min}}^{T_{\text{tr}}^{\max}} g_1(T) dT = - \frac{e}{1 - \frac{B_A}{B_0}} g_1(T_{\text{tr}}^{\min}) \tag{A.6}$$

by substituting Eqs. (A.15), (A.4) and

$$\frac{d}{dU_A}(T_{p,\max}) = 0. \quad (\text{A.7})$$

The integrand of the third integral, as well as the integration limits, do not depend U_A . Therefore we obtain

$$\frac{d}{dU_A}(r_h(U_A) \int_0^{T_{p,\max}} g_1(T)) = 0. \quad (\text{A.8})$$

By summing up Eq. (A.5), Eq. (A.6) and Eq. (A.8) we finally obtain:

$$\frac{d(\text{Numerator})}{dU_A} = - \int_{T_{\text{tr}}^{\min}}^{T_{\text{tr}}^{\max}} \frac{e}{2r_B T \sqrt{1 - \frac{B_0}{B_A} \left(1 - \frac{eU_A}{T}\right)}} g_1(T) dT \quad (\text{A.9})$$

The calculation for the derivative of the denominator of Eq. (2.12) with respect to U_A yields the same result, except for the proportionality to g_2 :

$$\frac{d(\text{Denominator})}{dU_A} = - \int_{T_{\text{tr}}^{\min}}^{T_{\text{tr}}^{\max}} \frac{e}{2r_B T \sqrt{1 - \frac{B_0}{B_A} \left(1 - \frac{eU_A}{T}\right)}} g_2(T) dT. \quad (\text{A.10})$$

Now we calculate the derivative of the numerator of Eq. (2.12) with respect to r_B .

$$\begin{aligned} \frac{d(\text{Numerator})}{dr_B} &= \frac{d}{dr_B} \underbrace{\left(\int_{T_{\text{tr}}^{\min}}^{T_{\text{tr}}^{\max}} \left(1 - \sqrt{1 - \frac{1}{r_B} \left(1 - \frac{eU_A}{T} \right)} \right) g_1(T) dT \right)}_{\text{I}} \\ &\quad + \underbrace{\int_{T_{\text{tr}}^{\max}}^{T_{\text{p,max}}} g_1(T) dT}_{\text{II}} - r_h(U_A) \underbrace{\int_0^{T_{\text{p,max}}} g_1(T)}_{\text{III}} \end{aligned} \quad (\text{A.11})$$

The upper integration limit of the first integral and the lower integration limit of the second integral are the same and depend on r_B . Therefore, we have to use Eq. (2.14) again:

$$\frac{d(\text{I})}{dr_B} = \frac{d}{dr_B} \left(\int_{T_{\text{tr}}^{\min}}^{T_{\text{tr}}^{\max}} \left(1 - \sqrt{1 - \frac{1}{r_B} \left(1 - \frac{eU_A}{T} \right)} \right) g_1(T) dT \right) \quad (\text{A.12})$$

$$= \int_{T_{\text{tr}}^{\min}}^{T_{\text{tr}}^{\max}} \frac{\partial}{\partial r_B} \left(1 - \sqrt{1 - \frac{1}{r_B} \left(1 - \frac{eU_A}{T} \right)} \right) g_1(T) dT \quad (\text{A.13})$$

$$\begin{aligned} &+ \frac{d}{dr_B} (T_{\text{tr}}^{\max}) (F_{\text{tr}}(T_{\text{tr}}^{\max}; r_B) g_1(T_{\text{tr}}^{\max})) \\ &- \frac{d}{dr_B} (T_{\text{tr}}^{\min}) (F_{\text{tr}}(T_{\text{tr}}^{\min}; r_B) g_1(T_{\text{tr}}^{\min})) \end{aligned} \quad (\text{A.14})$$

with the transmission function at the integration limits

$$F_{\text{tr}}(T_{\text{tr}}^{\min}; r_B) = 0$$

$$F_{\text{tr}}(T_{\text{tr}}^{\max}; r_B) = 1 \quad (\text{A.15})$$

and the derivatives of the integration limits

$$\frac{d}{dr_B} (T_{\text{tr}}^{\max}) = \frac{eU_A}{(1 - r_B)^2} \quad (\text{A.16})$$

$$\frac{d}{dr_B}(T_{\text{tr}}^{\text{min}}) = 0 \quad (\text{A.17})$$

this yields:

$$\frac{d(\mathbf{I})}{dr_B} = - \int_{T_{\text{tr}}^{\text{min}}}^{T_{\text{tr}}^{\text{max}}} \frac{1 - \frac{eU_A}{T}}{2r_B^2 \sqrt{1 - \frac{1}{r_B} \left(1 - \frac{eU_A}{T}\right)}} g_1(T) dT + \frac{eU_A}{(1 - r_B)^2} g_1(T_{\text{tr}}^{\text{max}}) \quad (\text{A.18})$$

The integrand of the second integral does not depend on r_B , but the lower integration limit does. Therefore, we get only one term

$$\frac{d(\mathbf{II})}{dr_B} = \int_{T_{\text{tr}}^{\text{max}}}^{T_{\text{p,max}}} g_1(T) dT = - \frac{eU_A}{(1 - r_B)^2} g_1(T_{\text{tr}}^{\text{max}}) \quad (\text{A.19})$$

The integrand of the third integral, as well as the integration limits, do not depend r_B . Therefore we obtain

$$\frac{d(\mathbf{III})}{dr_B} = \frac{d}{dr_B} \left(r_h(U_A) \int_0^{T_{\text{p,max}}} g_1(T) dT \right) = 0 \quad (\text{A.20})$$

By summing up Eq. (A.18), Eq. (A.19) and Eq. (A.20) we finally obtain:

$$\frac{d(\text{Numerator})}{dr_B} = - \int_{T_{\text{tr}}^{\text{min}}}^{T_{\text{tr}}^{\text{max}}} \frac{1 - \frac{eU_A}{T}}{2r_B^2 \sqrt{1 - \frac{1}{r_B} \left(1 - \frac{eU_A}{T}\right)}} g_1(T) dT$$

The calculation for the derivative of the denominator of Eq. (2.12) with respect to r_B yields the same result, except for the proportionality to g_2 :

$$\frac{d(\text{Denominator})}{dr_B} = - \int_{T_{\text{tr}}^{\text{min}}}^{T_{\text{tr}}^{\text{max}}} \frac{1 - \frac{eU_A}{T}}{2r_B^2 \sqrt{1 - \frac{1}{r_B} \left(1 - \frac{eU_A}{T}\right)}} g_2(T) dT$$

Appendix B

Data sheets and calibrations of the Hall-effect sensors

MPT-141

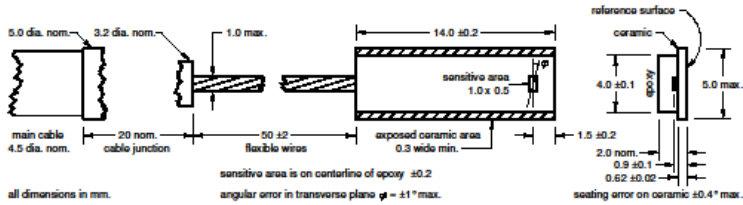
Group3

MINIATURE STANDARD SENSITIVITY HALL PROBE

- Very small sensitive area, small physical size.
 - Super high precision: $\pm 0.01\%$ max. error at 25 °C*.
 - Extremely low thermal drift: $\pm 5\text{ppm}/^\circ\text{C}$ max*.
 - Negligible zero drift: ± 0.01 gauss/°C max*.
 - Calibration tables at 0, 25 and 50 °C supplied with each probe.
- * contribution of probe only.

Specifications of system – MPT-141 with DTM-151 teslameter:

Orientation	Transverse, reads positive when field vector enters top epoxy surface																													
Field ranges	0.3 0.6 1.2 3.0 tesla full-scale, 3 6 12 30 kilogauss full scale with polarity indication, calibrated to ± 2.2 tesla, $\pm 22,000$ gauss																													
Accuracy at 25 °C	$\pm(0.01\%$ of reading $+0.006\%$ of full scale) max.																													
Resolution - DC mode with digital filtering ON:	1 in 600,000 of bipolar span in front panel display.																													
	<table border="1"> <thead> <tr> <th rowspan="2">range</th> <th colspan="2">display resolution</th> <th colspan="2">serial/GPIB resolution</th> </tr> <tr> <th>gauss</th> <th>tesla</th> <th>gauss</th> <th>tesla</th> </tr> </thead> <tbody> <tr> <td>0.3 tesla</td> <td>0.01</td> <td>0.000001</td> <td>0.001</td> <td>0.0000001</td> </tr> <tr> <td>0.6 tesla</td> <td>0.02</td> <td>0.000002</td> <td>0.01</td> <td>0.000001</td> </tr> <tr> <td>1.2 tesla</td> <td>0.04</td> <td>0.000004</td> <td>0.01</td> <td>0.000001</td> </tr> <tr> <td>3.0 tesla</td> <td>0.1</td> <td>0.00001</td> <td>0.01</td> <td>0.000001</td> </tr> </tbody> </table>	range	display resolution		serial/GPIB resolution		gauss	tesla	gauss	tesla	0.3 tesla	0.01	0.000001	0.001	0.0000001	0.6 tesla	0.02	0.000002	0.01	0.000001	1.2 tesla	0.04	0.000004	0.01	0.000001	3.0 tesla	0.1	0.00001	0.01	0.000001
range	display resolution		serial/GPIB resolution																											
	gauss	tesla	gauss	tesla																										
0.3 tesla	0.01	0.000001	0.001	0.0000001																										
0.6 tesla	0.02	0.000002	0.01	0.000001																										
1.2 tesla	0.04	0.000004	0.01	0.000001																										
3.0 tesla	0.1	0.00001	0.01	0.000001																										
Resolution - DC mode with digital filtering OFF, and AC mode:	1 in 120,000 of bipolar span in front panel display.																													
	<table border="1"> <thead> <tr> <th rowspan="2">range</th> <th colspan="2">display resolution</th> <th colspan="2">serial/GPIB resolution</th> </tr> <tr> <th>gauss</th> <th>tesla</th> <th>gauss</th> <th>tesla</th> </tr> </thead> <tbody> <tr> <td>0.3 tesla</td> <td>0.05</td> <td>0.000005</td> <td>0.001</td> <td>0.0000001</td> </tr> <tr> <td>0.6 tesla</td> <td>0.1</td> <td>0.00001</td> <td>0.01</td> <td>0.000001</td> </tr> <tr> <td>1.2 tesla</td> <td>0.2</td> <td>0.00002</td> <td>0.01</td> <td>0.000001</td> </tr> <tr> <td>3.0 tesla</td> <td>0.5</td> <td>0.00005</td> <td>0.01</td> <td>0.000001</td> </tr> </tbody> </table>	range	display resolution		serial/GPIB resolution		gauss	tesla	gauss	tesla	0.3 tesla	0.05	0.000005	0.001	0.0000001	0.6 tesla	0.1	0.00001	0.01	0.000001	1.2 tesla	0.2	0.00002	0.01	0.000001	3.0 tesla	0.5	0.00005	0.01	0.000001
range	display resolution		serial/GPIB resolution																											
	gauss	tesla	gauss	tesla																										
0.3 tesla	0.05	0.000005	0.001	0.0000001																										
0.6 tesla	0.1	0.00001	0.01	0.000001																										
1.2 tesla	0.2	0.00002	0.01	0.000001																										
3.0 tesla	0.5	0.00005	0.01	0.000001																										
Temperature range	0 to 50 °C operating to spec, -20 to +60 °C max.																													
Temperature stability	calibration: $\pm 10\text{ppm}$ of reading/°C max. -3ppm/°C of reading per meter of probe cable zero drift: $\pm(1\mu\text{T} + 0.0003\%$ of full-scale)/°C max.																													
Probe dimensions	overall size: 14 x 5 x 2 mm sensitive area: 1 x 0.5mm unshielded part of cable at probe head: 4.5mm diam. 300mm nom. length shielded cable: 6.5mm diam.																													
Order code	MPT-141-2s for probe with basic 2 meter shielded cable. Special probe cable lengths may be ordered up to 30 meters max. Single-range probes: add range suffix -03 -06 -12 -30, e.g. MPT-141-03-2s.																													



all dimensions in mm.

Group3 reserves the right to change specifications at any time without notice.

Group3 Technology Ltd. www.group3technology.com info@group3technology.com

file: MPT-141spec.doc May 2005 84000181

Figure B.1: Data sheet of the MPT-141 Hall-effect sensor



SCHAEFER TECHNOLOGIE GMBH

Mörfelder Landstraße 33
D - 63225 Langen
Tel. (06103) 3 00 98-0 · Fax (06103) 3 00 98-29
E-mail: info@schaefer-tec.com
www.schaefer-tec.com

Please find below calibration information as requested for your order 210/06-418/1/06 DTM-151-DG Serial Number 01350084

Previous Calibration Information: 2002

Zero's	Scales	Actual Zero	Actual Field Scales
Range 0: 1.757	Range 0: 1.00662E0	Range 0: -0.36	Range 0: 2997.18
Range 1: 2.76	Range 1: 1.00612E0	Range 1: -0.44	Range 1: 5995.74
Range 2: 4.54	Range 2: 1.00538E0	Range 2: -0.68	Range 2: 11996.04
Range 3: 9.56	Range 3: 1.00506E0	Range 3: -2.2	Range 3: 29988.7

Temperature:

Zero
-2.1
Scale
1.03291E0

New Calibration Information: 2006

Zero's	Scales
Range 0: 2.106	Range 0: 1.00757E0
Range 1: 3.20	Range 1: 1.00684E0
Range 2: 5.23	Range 2: 1.00571E0
Range 3: 11.57	Range 3: 1.00544E0

Temperature

Zero
-2.1
Scale
1.03331E0

Figure B.2: 2006 calibration of the MPT-141 Hall-effect sensor.

F_u	Uncorrected field reading
F_{c1}	Corrected field reading (original calibration)
F_{c2}	Corrected field reading (new calibration)
Z_1	Original zero offset
C_1	Original scale factor
Z_2	New zero offset
C_2	New scale factor

Original corrected field readings:

$$F_{c1} = C_1 \times (F_u + Z_1)$$

Therefore:

$$F_u = F_{c1}/C_1 - Z_1$$

New Corrected field reading =

$$F_{c2} = C_2 \times (F_u + Z_2) \quad \text{- where } F_u = F_{c1}/C_1 - Z_1 \text{ (above)}$$

Therefore:

$$F_{c2} = C_2 \times (F_{c1}/C_1 - Z_1 + Z_2)$$

Note 1: Z_1 , Z_2 , C_1 & C_2 change according to the range in use at the time.

Note 2: DTM zeros are in gauss

For example,

Instrument originally measures 1.500 T = 15000 g

Assume that Range-3 is in effect

$$\begin{aligned} \text{New corrected field} &= 1.00544 \times (15000/1.00506 - 9.56 + 11.57) \\ &= 15008\text{g} \end{aligned}$$

Figure B.3: Continuation of Fig. B.2.

1.) Field point: 21.53 Gauss (2.1mT)
Actual Reading:
R0: 19.22 G
R1: 19.16 G
R2: 19.20 G
R3: 20.6 G

2.) Field point: 4000.68 Gauss (400mT)
Actual Reading:
R0: over range
R1: 4003.70 G
R2: 4002.08 G
R3: 4001.6 G

3.) Field point: 21014.2 Gauss (2.1 T)
Actual Reading:

R3: 21002.8 Gauss

The probe was tested at 25 degrees C.

Figure B.4: 2011 calibration of the MPT-141 Hall-effect sensor.



Form No.SCH-TR-01350084-1

DTM Repair and Calibration Report

Customer	Schaefer	DTM Model	DTM-151-DG
Date Received	03 December 2013	Serial Number	01350084
Due Date	ASAP	RMA Number	280/13-418/4/13
Customer Notes:			

INITIAL ASSESSMENT

I. Physical:

Serial Board: Good ✓ Fail ___
 Analog Board: Good ✓ Fail ___
 Communication Port: Good ✓ Fail ___
 Power supply: Good ✓ Fail ___
 Case: Good ✓ Fail ___
 Front and back Panel: Good ✓ Fail ___

Software Version: V 6.0b 24 October 2001
 Analogue Board S/II 836
 GPIB Board S/II 085
 DIP Switch Setting: SW1: ON- 2
 SW2: ON- 1, 2, 5

Comment:
G3:

II. Calibration:

Current Calibration Factors

	ROIZ	R1IZ	R2IZ	R3IZ	Temp.
MFG Zero	2.106	3.20	5.23	11.57	-2.1
Scale	1.00757	1.00684	1.00571	1.00544	1.03331

Measured Against A Probe: Reference Field: 0 Gauss

DTM Reading

Range 0 4.12 Gauss
 Range 1 6.10 Gauss
 Range 2 10.96 Gauss
 Range 3 7.0 Gauss

Reference Temperature: 24°C
 Actual Temperature: 24.4

Comment:

G3: Field calibrations on all ranges are a bit off.

Figure B.5: 2013 calibration of the MPT-141 Hall-effect sensor.



Form No.SCH-PR-01231572-02

Probe Repair and Calibration Report

Customer	Schaefer Germany	Probe Model	MPT-141-105
Date Returned	02 December 2013	Serial Number	01231572
Due Date	13 December 2013	RMA Number	280/13-418/4/13
Customer notes:	"Customer needs both the new calibration table after potential adjustments, but also wants that he gets the table of how the instrument performs now, as received, before recalibration, so they can know how good the measurements may have been they did until now"		

INITIAL ASSESSMENT

I. Physical:

Probe Head: Good ✓ Fail ___
 Plug Case: Good ✓ Fail ___
 Probe Board/Pin: Good ✓ Fail ___
 Cable: Good ✓ Fail ___

G3 Comment: no physical defects seen on unit

II. Calibration:

Calibration Readings:

Below is the probe performance as compared with the reference (in GAUSS):

Reference	Range 0.3T	Range 0.6T	Range 1.2T	Range 3.0T
182.55	182.25	182.42	182.36	182.2
585.88	585.63	585.62	585.52	585.3
1016.63	1016.34	1016.36	1016.28	1016.2
1960.17	1959.52	1959.64	1959.52	1959.4
3027.54	3026.55	3026.50	3026.44	3026.4
6036.14	-----	6033.78	6033.76	6033.6
12637.50	-----	-----	12630.24	12630.5
22361.88	-----	-----	-----	22343.5

Temperature Readings:

Reference Temperature Reading (A3): 25.0°C
 Actual Probe Temperature Reading: 23.9°C

FINAL ASSESSMENT

Figure B.6: Continuation of Fig. B.5.

ELECTRICAL SPECIFICATIONS OF THE HALL PROBE

HIGH LINEARITY HALL PROBE FOR ROOM AND CRYOGENIC
TEMPERATURES

TYPE: **HHP-SF** PRODUCT NUMBER: **662**

PARAMETER	UNIT	300 K	77 K	4.2 K
Nominal control current, I_n	mA	5	5	5
Maximum control current	mA	6	10	10
Sensitivity at I_n	mV/T	29.3		
Offset voltage at I_n	μ V	< -120	< 80	
Input resistance	Ω	103	111	
Output resistance	Ω	100	105	
Linearity error up to 1 T	%	< 0.2		
Change of sensitivity due to reversing of the magnetic field	%	< 1		

Active area dimensions [mm]: 0.02 x 0.02
Overall dimensions [mm]: \varnothing 5 x 8

COLOR CODE:

Control current leads: green, black
Hall leads: orange, red

AREPOC s.r.o., Iljusinova 4, 851 01 Bratislava, SLOVAKIA
FAX: +421 2 6382 4613 E-mail: kopera@arepoc.sk
<http://www.arepoc.sk>

Figure B.7: Data sheet of HHP-SF 662

Bibliography

- [1] GROUP 3 TECHNOLOGY LTD. <http://www.group3technology.com/dlarea/docs/MPT-141%20spec.pdf>.
- [2] AREPOC S.R.O. <http://www.arepoc.sk/uploaded/download/HallProbes.PDF>.
- [3] ASPECT COLLABORATION, *conference call*. 11th Dec 2012.
- [4] F. AYALA GUARDIA, *First Tests of the neutron decay spectrometer aSPECT*, master's thesis, Johannes Gutenberg-Universität Mainz, 2005.
- [5] —, *Calibration of the retardation spectrometer aSPECT*, PhD thesis, Johannes Gutenberg-Universität, Mainz, 2011.
- [6] S. BAESSLER ET AL., *First measurements with the neutron decay spectrometer aSPECT*, Eur. Phys. J. A, 38 (1) (2008), pp. 17–26.
- [7] J. BERINGER ET AL., (*Particle Data Group*), Phys. Rev. D, 86 (2012), p. 010001. and 2013 partial update for the 2014 edition (URL: <http://pdg.lbl.gov>).
- [8] M. BORG, *The electron antineutrino angular correlation coefficient a in free neutron decay: Testing the Standard Model with the aSPECT-Spectrometer*, PhD thesis, Johannes Gutenberg-Universität, Mainz, 2010.
- [9] R. N. CAHN, *The eighteen arbitrary parameters of the Standard Model in your everyday life*, Rev. Mod. Phys, 68 (1996), pp. 951–959.
- [10] COMSOL, INC. <http://www.comsol.com/comsol-multiphysics>.
- [11] W. N. COTTINGHAM AND D. A. GREENWOOD, *An Introduction to the Standard Model of Particle Physics*, Cambridge University Press, Cambridge, second ed., 2007.

- [12] P. DAWBER ET AL., Nucl. Instr. and Meth., A 440 (2000), p. 543.
- [13] A. O. EARLS, I. P. AXFORD, AND J. H. BRAYBROOK, *Gas chromatography-mass spectrometry determination of the migration of phthalate plasticisers from polyvinyl chloride toys and childcare articles*, J. Chromatography A, 983 (2003), pp. 237–246.
- [14] F. EURICH, *Aufbau eines Versuchs zur Restgasanalyse*, master’s thesis, Goethe-Universität, Frankfurt am Main, 1998.
- [15] F. GLÜCK, Phys. Rev., D 47 (1993), p. 2840.
- [16] —, *The penning discharge*. Summary of literature, 2007.
- [17] F. GLÜCK ET AL., *Measurable parameters of neutron decay*, Nucl. Phys. A, 593 (1995), p. 125.
- [18] —, *The neutron decay retardation spectrometer aSPECT: Electromagnetic design and systematic effects*, Eur. Phys. J. A, 23 (2005), p. 135.
- [19] C. HABECK, *PHD thesis*, PhD thesis, University of Sussex, 1997.
- [20] G. HINSHAW ET AL., *Nine-Year Wilkinson Microwave Anisotropy Probe (WMAP) Observations: Cosmological Parameter Results*, Astrophys. J. Suppl. Ser., 208 (2) (2013), p. 19. arXiv:1212.5226v3 [astro-ph.CO].
- [21] J. D. JACKSON, S. B. TREIMAN, AND H. W. WYLD, *Possible tests of time reversal invariance in beta decay*, Phys. Rev., 106 (1957), p. 517.
- [22] G. KONRAD, *private communication*, 2013.
- [23] G. E. KONRAD, *Measurement of the Proton Recoil Spectrum in Neutron Beta Decay with the Spectrometer aSPECT: Study of Systematic Effects*, PhD thesis, Johannes Gutenberg-Universität, Mainz, 2011.
- [24] R. MAISONOBE, PhD thesis, Université Joseph Fourier, Grenoble. in progress.
- [25] —, *private communication*, 2013.
- [26] R. MAISONOBE ET AL., *Background investigations of the neutron β -decay spectrometer aSPECT*, in PSI 2013 Workshop, September 8-12 2013, PSI Villigen, Switzerland, 2013.

- [27] R. MUÑOZ HORTA, *First measurements of the aSPECT spectrometer*, PhD thesis, Johannes Gutenberg-Universität, Mainz, 2011.
- [28] O. NACHTMANN, *Z. Phys.*, 215 (1968), p. 505.
- [29] L. PAPULA, *Mathematik für Ingenieure und Naturwissenschaftler, Band 3*, Vieweg, Braunschweig, fourth ed., 2001.
- [30] R. PECCEI AND H. R. QUINN, *CP conservation in the presence of pseudoparticles*, *Phys. Rev. Lett.*, 38 (1977), pp. 1440–1443.
- [31] A. PICARD ET AL., *Nucl. Instr. and Meth.*, B 63 (1992), p. 345.
- [32] M. SIMSON, *Measurement of the electron antineutrino angular correlation coefficient a with the neutron decay spectrometer aSPECT*, PhD thesis, Technische Universität, München, 2010.
- [33] O. ZIMMER, *V_{ud} from neutron beta decay*, arXiv: 1301.1854, (2013).
- [34] O. ZIMMER ET AL., *Nucl. Instr. and Meth.*, A 440 (2000), p. 548.

Acknowledgements

I take this opportunity to express my thanks to all the people that supported me throughout the last months. I am particularly grateful for the assistance given by my supervisors. Furthermore, I wish to acknowledge the help provided by all other members of the Institute of Atomic and Subatomic Physics . Last but not least, I like to thank all my family and friends for great quarter of a century.